The Journal of Experimental Biology 206, 725-744

doi:10.1242/jeb.00137

Hydrodynamic stability of swimming in ostraciid fishes: role of the carapace in the smooth trunkfish *Lactophrys triqueter* (Teleostei: Ostraciidae)

Ian K. Bartol[1,*], Morteza Gharib[2], Daniel Weihs[3], Paul W. Webb[4], Jay R. Hove[2] and Malcolm S. Gordon[1]

[1]*Department of Organismic Biology, Ecology, and Evolution, University of California, Los Angeles, CA 91606, USA,* [2]*Options of Bioengineering and Aeronautics, California Institute of Technology, Pasadena, CA 91125, USA,* [3]*Department of Aerospace Engineering, Technion, Haifa, 3200, Israel* and [4]*School of Natural Resources and Department of Biology, University of Michigan, Ann Arbor, MI 48109, USA*

*Author for correspondence (e-mail: ikbartol@lifesci.ucla.edu)

Accepted 11 November 2002

Summary

The hydrodynamic bases for the stability of locomotory motions in fishes are poorly understood, even for those fishes, such as the rigid-bodied smooth trunkfish *Lactophrys triqueter*, that exhibit unusually small amplitude recoil movements during rectilinear swimming. We have studied the role played by the bony carapace of the smooth trunkfish in generating trimming forces that self-correct for instabilities. The flow patterns, forces and moments on and around anatomically exact, smooth trunkfish models positioned at both pitching and yawing angles of attack were investigated using three methods: digital particle image velocimetry (DPIV), pressure distribution measurements, and force balance measurements. Models positioned at various pitching angles of attack within a flow tunnel produced well-developed counter-rotating vortices along the ventro-lateral keels. The vortices developed first at the anterior edges of the ventro-lateral keels, grew posteriorly along the carapace, and reached maximum circulation at the posterior edge of the carapace. The vortical flow increased in strength as pitching angles of attack deviated from 0°, and was located above the keels at positive angles of attack and below them at negative angles of attack. Variation of yawing angles of attack resulted in prominent dorsal and ventral vortices developing at far-field locations of the carapace; far-field vortices intensified posteriorly and as angles of attack deviated from 0°. Pressure distribution results were consistent with the DPIV findings, with areas of low pressure correlating well with regions of attached, concentrated vorticity. Lift coefficients of boxfish models were similar to lift coefficients of delta wings, devices that also generate lift through vortex generation. Furthermore, nose-down and nose-up pitching moments about the center of mass were detected at positive and negative pitching angles of attack, respectively. The three complementary experimental approaches all indicate that the carapace of the smooth trunkfish effectively generates self-correcting forces for pitching and yawing motions – a characteristic that is advantageous for the highly variable velocity fields experienced by trunkfish in their complex aquatic environment. All important morphological features of the carapace contribute to producing the hydrodynamic stability of swimming trajectories in this species.

Key words: boxfish, *Lactophrys triqueter*, stability, hydrodynamics, swimming, pressure, particle image velocimetry, moment.

Introduction

Hydrodynamic stability, as applied to moving, aquatic animal systems, may be best defined as the control and regulation of trajectories during steady and intentional unsteady motions of maneuvers, such that the body resists movement from an original state, returns readily to an original state, or maintains a desired path after and/or while being affected by external and self-generated perturbations (Weihs, 1993, 2002; Webb, 2000, 2002). In the water column, a common external perturbation is turbulence, which may be biotic (e.g. wakes of other fishes) or abiotic (e.g. flow at interfaces and over topographic features like coral and boulders) in origin. Self-generated perturbations may involve buoyancy forces, gill ventilation and locomotor movements. Hydrodynamic stability control arises from flow over the body and appendages and is achieved by trimming and powered correction systems. In trimming correction systems, control surfaces (effectors) move with the body and are positioned to self-correct a disturbance and/or passively damp the rate of growth of perturbations (e.g. paired fins extended at a positive dihedral angle to self-correct for rolling perturbations) (Aleyev, 1977; Weihs, 1989, 1993; Webb, 2002). Powered correction systems, as the name suggests, involve active

movement of the effectors independent of the body to correct disturbances (e.g. asymmetrical pectoral fin beats to correct a rolling moment) (Webb, 2000, 2002).

Powered correction systems are used by many fishes under a multitude of conditions to regulate trajectories. For powered systems, neural processing is required before the effectors make corrections and may ultimately be the limiting factor for actively regulating trajectories (Webb, 2000). Many disturbances, especially those that are external, have low predictability in terms of direction, period or amplitude. Under these conditions, accurate phasing of correction forces with perturbations is difficult. Without proper phasing, correction may even amplify the disturbance through 'pilot-induced error' (Webb, 1998, 2000). Trimming self-correcting systems, on the other hand, can accommodate these unpredictable events more effectively, since response latency periods are not required. Consequently, fish relying more heavily on trimming control seemingly are better adapted to more turbulent regimes than fish emphasizing powered-control systems. Support for this hypothesis is provided by Webb (1998), who discovered that the smallmouth bass *Micropterus dolomieu*, a fish that relies heavily on powered control, has greater difficulty holding station in the wake of cylinders than the river chub *Nocomis micropogon*, a fish that relies heavily on self-correcting trimming control.

Whether using trimming or powered hydrodynamic systems, controlling trajectories and avoiding growth of disturbances into energy-wasting displacements is essential to organisms for effective and economical swimming. However, surprisingly little is known about stability of locomotory motions in fishes and other aquatic organisms, as noted by Blake (1981), Weihs (1993, 2002) and Webb (2000, 2002). An intriguing fish that resides in a highly turbulent environment and may take advantage of both trimming and powered control is the smooth trunkfish *Lactophrys triqueter*. The smooth trunkfish is a neotropical reef-dwelling fish that has a rigid bony carapace consisting of hexagonal plates (or scutes), which encases about 70–75% of its body (Tyler, 1980). The carapace, a feature that distinguishes it from most flexible-bodied marine fishes, is predominantly triangular in cross-section, with one dorsal and two prominent ventro-lateral keels (Fig. 1). In smooth trunkfishes and other marine boxfishes (Teleostei: Ostraciidae), the carapace limits body movements to locations posterior to the caudal peduncle. As a result, these fishes rely heavily on complex combinations of movement of their five fins for swimming.

Field observations and recent studies on the swimming physiology of boxfishes indicate that they are capable of remarkably low recoil motions, both when moving in flumes and in highly variable velocity fields in nature, resulting in smooth, energy-efficient, rectilinear swimming trajectories (Gordon et al., 2000; Hove et al., 2001). Although there are some studies describing and analyzing swimming in rigid-bodied ostraciiform fishes (Blake, 1977, 1981, 1983a,b; Hove et al., 2001), little is known about how this remarkable stability is achieved. The objective of our study was to understand what role the uniquely shaped carapace of the smooth trunkfish plays in maintaining this stability. We were particularly interested in trimming self-correcting forces for pitching and yawing.

We approached this objective using three separate but interrelated techniques. For each approach, an anatomically exact, stereolithographic model of the smooth trunkfish was used. The three techniques applied were: (1) digital particle image velocimetry (DPIV), which provides a global picture of flow structures at various planes along the carapace; (2) pressure distribution measurements, which provide information on what is happening at the surface of the carapace, a region that is difficult to resolve using DPIV; and (3) force balance measurements, which provide an integrated view of forces acting on the carapace.

Materials and methods

Model construction

One *Lactophrys triqueter* L. (17.0 cm total length, 128.8 g) was captured by hook and line in Puerto Rico, frozen immediately, and shipped to the University of California, Los Angeles (UCLA), where it was stored in a –70°C freezer until it was prepared for computerised tomography (CT) scanning. This specimen was in excellent condition and had carapace features that closely resembled those of smooth trunkfish considered in other studies conducted in our laboratory. Preparation protocol involved removing the dorsal and anal fins, positioning the pectoral fins flush against the body, and aligning the caudal fin with the longitudinal axis of the fish. Once the exterior of the carapace was thawed completely, the specimen was dried off with a towel and placed on a low-density block of Styrofoam (floral frog). The Styrofoam block elevated the fish above the scanner bed during CT scanning, which made it easier to distinguish ventral portions of the carapace from the bed in cross-sectional exposures.

The specimen was scanned using a GE CT/i high-speed scanner (General Electric Medical Systems, Milwaukee, WI, USA). A continuous scan was performed through the entire fish using a 1.0 mm collimation at 120 kVp/200 mA^{-1} and a 1 s rotation time. A 50% overlap was used so that images were reconstructed every 0.5 mm. A total of 340 consecutive, two-dimensional (2-D), cross-sectional exposures were generated longitudinally from the snout to the posterior edge of the caudal fin. An appropriate threshold (contrast) was selected for maximum resolution of the carapace, and the images were converted to digital stereolithography (STL) files using a Marching Cubes algorithm, a high-resolution 3-D surface construction algorithm (Lorensen and Cline, 1987). Exact 3-D physical models of polymerized epoxy resin, one in halves and the other whole, were created from the files using stereolithographic rapid-prototyping (Solid Concepts, Inc., Valencia, CA, USA).

Measurements of CT images

A variety of morphological measurements were collected from the 2-D, cross-sectional CT images to characterize the unique shape of the carapace. Before measurements were

taken, the CT images were converted from a UCLA PACS in-house format to a TIFF format. Measurements were collected from every fourth image using NIH Image v. 1.61 (National Institute of Health, http://rsb.info.nih.gov/nih-image/). For each CT image considered, carapace width (distance from ventro-lateral keel tip to ventro-lateral keel tip), carapace height (distance from dorsal keel tip to midline of ventral region), eye ridge width (distance from eye ridge tip to edge ridge tip), dorsal keel angle (determined using the apex of the keel (vertex) and the two widest points on either side of keel apex), and both ventro-lateral keel angles (determined similarly to dorsal keel angles) were measured along the length of the carapace (Fig. 1). To characterize levels of lateral and ventral concavity/convexity, a segment connecting the apex of each ventro-lateral keel and the apex of the dorsal keel (S_L) and a segment connecting the apices of the ventro-lateral keels (S_V), respectively, were drawn on all CT images considered using NIH image. The maximum distance(s) the body indented and/or extended relative to the segment and location(s) of maximum indentation/extension along the segment were recorded.

Digital particle image velocimetry

Willert and Gharib (1991) and Raffel et al. (1998) provide detailed descriptions of the DPIV technique for flow field measurements. A general description of the experimental techniques relevant to our study is given here. To reduce glare from laser light, one of the two fabricated models was painted black, which did not obscure the hexagonal scute topography at the surface of the carapace. For DPIV measurements made along the body, the tail of the model was removed and replaced with a 10 cm rod (also painted black and 1.0 cm in diameter, which was similar in dimension to the caudal peduncle). The rod was connected to a sting that entered the water tunnel from above. For DPIV measurements in the wake, the tail was reattached, and the sting was affixed to a machined connector located at the caudal peduncle. We used a water tunnel with a 30 cm×30 cm×100 cm test section (Model 503, Engineering Laboratory Design, Inc., Lake City, MN, USA) seeded with silver-coated hollow glass spheres (14 μm in diameter). Two pulsed ND:YAG lasers (wavelength=532 nm, power rating 50 mJ; New Wave Research, Fremont, CA, USA), a series of front-surface mirrors, and a cylindrical lens were used to generate and align an illuminated sheet approximately 1.0 mm thick. The laser sheet was projected beneath the water tunnel in a transverse (*YZ*) plane. A Pulnix CCD video camera (TM-9701) with a frame size of 480×768 pixels and frame rate of 30 Hz was positioned downstream of the working section (unobstructed views of oncoming flow were made possible through a Plexiglas exit tank).

The video camera, lasers and a Coreco OC-TC10-DIGSE frame grabber (National Instruments, Inc., Austin, TX, USA) were synchronized using a video timing box and *FlowVision*^{TM} software (PixelFlow, Pasadena, CA, USA). The video camera generated timing signals for phase-locking the frame grabber, lasers and camera. Generally, the two lasers were pulsed for 0.02 ms and separated by a period of 1 ms during paired image collection. At least 60 sequential images (30 paired images) were considered for processing for each trial. In all images except those collected in the wake, the model was subtracted out of the video image prior to processing. The interrogation window (i.e. the area over which the particle shifts were averaged) was 32^2 pixels with a 16 pixel offset (50% overlap). The displacement of particles within the interrogation windows comprising the paired images was calculated using cross-correlation (Willert and Gharib, 1991). Outliers, defined as particle shifts that were 3 or more pixels greater than particle shifts of neighboring particles, were removed and corrected, and data were smoothed to remove high frequency fluctuations within the video images.

The resulting flow displacement fields were divided by the time difference between the paired images to determine the velocity field of the flow. Mean velocity and mean vorticity fields were determined for each trial using *FlowVision*^{TM} software. Circulation of regions of concentrated vorticity attached to the model was determined by carefully tracing along the outline of the model where the region of concentrated vorticity was present, tracing along the remaining vorticity contour found external to the model, and then computing the area integral within the tracing using an in-house code at the California Institute of Technology. Circulation of vortices in the wake was determined by tracing along the outlines of each region of concentrated vorticity and computing the area integral of the tracing.

DPIV measurements were collected at transverse planes along the length and within the wake of the model as it was positioned at various pitching angles of attack in the water tunnel. The water tunnel was set at a speed of 44 cm s^{-1} (2.6 *BL* s^{-1}), where *BL*=body length, which corresponds to roughly half the sustained speed range of boxfish (J. Hove, unpublished swim tunnel data). The water tunnel was also set at low speeds (10 cm s^{-1}, 0.6 *BL* s^{-1}) and high speeds (90 cm s^{-1}, 5.3 *BL* s^{-1}) periodically to confirm that DPIV results at the intermediate speed were qualitatively applicable over the range of swimming speeds of the fish. Data were collected at 2° intervals between –10 and +10°, and at 5° intervals at more negative and positive angles of attack, up to –30 and +30°, respectively. At all pitching angles of attack, flow patterns were examined in the wake of the model (5 cm downstream from the caudal fin) and at five locations along the body of the model: the eye ridge, the point of maximum girth, the midpoint between the point of maximum girth and the posterior edge of the carapace, the posterior edge of the carapace and the caudal peduncle. Several (2–3) trials were performed at each location at each pitching angle of attack. The model was oriented sideways, upside-down, and right-side-up in the water tunnel during the various angles of attack to ensure that no zones around the carapace were ignored because of shadowing. The upside-down orientation worked best for positive pitching angles, while the sideways orientation worked best for negative pitching angles. Lift on the carapace was computed at each angle of attack considered using a 2-D airfoil lift equation

(Tritton, 1998): $L_s=-\rho_W u\Gamma$, where L_s is lift per unit span ($kg\,s^{-2}$), ρ_W is freshwater density ($kg\,m^{-3}$), u is flow speed ($m\,s^{-1}$), and Γ is mean circulation of each vortex comprising the pair in the wake of the model ($m^2\,s^{-1}$). These vortices represent both the linear and non-linear contributions to slender wing-body lift (Küchemann, 1978). To obtain total lift L, L_s was multiplied by the span of the ventral region of the boxfish model.

Additional DPIV studies were performed at transverse planes along the length of the model as it was positioned at various yawing angles of attack (0 to +30°) in the water tunnel set at the same speed described above. Data were collected at yawing angles of attack of 0, 10, 20 and 30° at the following locations: the eye ridge, the point of maximum girth, the midpoint between the point of maximum girth and the posterior edge of the carapace, the posterior edge of the carapace, and caudal peduncle. Several (2–3) trials were performed at each location at each yawing angle of attack. As was the case for pitching studies, the models were positioned in different orientations to ensure that no shadowed region was overlooked. The upside-down orientation worked best for yawing studies.

Pressure measurements

The second smooth trunkfish model, constructed in halves but identical in dimensions to that employed in DPIV experiments, was used for pressure experiments. One of the model halves was hollowed out, and 36 holes were drilled in lateral and ventral regions of the carapace. The holes were drilled along body transects similar to those examined in the DPIV studies. Urethane tubing (i.d. 0.068 cm, o.d. 0.129 cm) was inserted into the holes and glued in place so that the tubing was flush with the model surface. The two model halves were glued together. Tubing exited the model through a 1.0 cm diameter, 10 cm long rod attached to the posterior section of the model. The rod was used to mount the model to a sting in a 61 cm wind tunnel (model 407, Engineering Laboratory Design, Inc., Lake City, MN, USA). Tubing exiting the model was connected to a Scanivalve 48-channel rotating pressure scanner (Scanivalve Inc., Liberty Lake, WA, USA) and a barocel electric manometer and capacitative differential pressure sensor (Barocel Datametrics, Wilmington, MA, USA). Static pressure ($N\,m^{-2}$) at each of the 36 ports was expressed relative to static pressure ($N\,m^{-2}$) at a tunnel wall port.

Data were collected while each model was positioned at 2° intervals for pitching angles of attack of –30 to +30° and yawing angles of attack of 0 to 30° (for yawing angles of attack the pressure ports were both exposed to flow (i.e. positioned in the near field carapace side) and shielded from flow (i.e. positioned in the far field carapace side) for each of the angles of attack). For the angles considered, data were acquired at 100 Hz for 10 s using LabVIEW software (National Instruments, Inc.). Wind tunnel speed was set according to the Reynolds number considered in water tunnel trials. Pressure coefficients (C_P) were calculated by dividing the pressure difference above ($N\,m^{-2}$) by dynamic pressure [$\rho_A U^2/2$; where ρ_A is air density ($kg\,m^{-3}$) and U is wind speed ($m\,s^{-1}$)], determined using a Pitot-static tube positioned in the wind tunnel.

Force measurements

The smooth trunkfish model used in DPIV experiments was also used in force measurement experiments. The model was mounted caudally to a sting in a water tunnel with a test section 61 cm×46 cm×244 cm in dimension. Force measurements were collected using three Interface 2.27 kg strain gauge load cells (Interface, Inc. Scottsdale, AZ, USA) [two load cells measured forces normal to flow (lift), one load cell measured forces parallel to flow (drag)] connected to an in-house force balance (Lisoski, 1993). Data output from the load cells were amplified using three Interface SGA amplifiers/conditioners and recorded with a Dash 8 Series data recorder (Astro-Med, Inc.). Data were collected at 200 Hz for 10 s for each angle considered. As was the case for pressure experiments, force data were collected every 2° from pitching angles of attack of –30 to +30° (some additional angles <–30° and >+30° were also considered). Flow speed during trials was identical to that considered in DPIV experiments [44 cm s^{-1} (2.6 $BL\,s^{-1}$)].

Coefficients of drag (C_D) and lift (C_L) were calculated using steady-state equations [$C_D=2\times D/(\rho_W\times A_f\times u^2)$ or $C_L=2\times L/(\rho_W\times A_p\times u^2)$, where D is total drag (N), L is total lift (N), ρ_W is water density ($kg\,m^{-3}$), A_f is maximum frontal area (m^2), A_p is planform surface area of the ventral region of

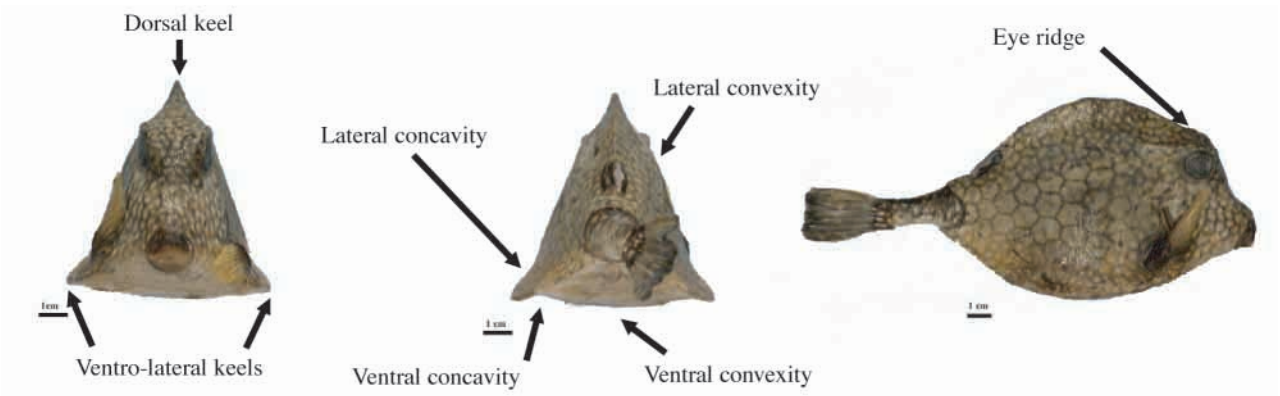

Fig. 1. Anterior, posterior and lateral views of a smooth trunkfish *Lactophrys triqueter*. Scale bars, 1 cm.

the carapace (m^2), and u is water tunnel speed ($m\,s^{-1}$)]. Pitching moments (M) about the center of mass of the models were computed using the equation: $M=d_1(L_2–L_1)+(L_1+L_2)\times(d_2\cos\alpha)+D(d_2\sin\alpha)$, where d_1 is distance (m) between load cell beams in the force balance, d_2 is distance (m) between center of force balance and center of mass of model, L_1 is lift (N) measured at load cell closest to model, L_2 is lift (N) measured at load cell farthest from model, D is drag (N) on the model, and α is angle of attack (degrees) of the model. Pitching moment coefficients (C_M) were computed using the equation: $C_M=2M/(\rho_W A_p c U^2)$, where c is the chord length of carapace (m).

Results

Measurements of CT images

The carapace of the smooth trunkfish is predominantly triangular in cross-section, has no significant ornamentation, and has 1 dorsal and 2 ventro-lateral keels (Fig. 1). Maximum body width (6.4 cm) and maximum body height (7.1 cm) of the scanned smooth trunkfish specimen occurred at locations 51% and 48% of carapace length *CL*, respectively (37% and 35% of the total length *TL* of the fish, respectively) (Fig. 2). The eye ridge, which was fairly consistent in width (1.8–2.0 cm) at most of the transverse sections where it was present, began at a location 14% *CL* and ended at 37% *CL*. Ventro-lateral keels were first noticeable at a location 14% *CL* as well. At this anterior region of the carapace, the ventro-lateral keels were broad (140°) and rounded, but then sharpened posteriorly down to an angle of 24° at a position 82% *CL*. At locations >82% *CL*, ventro-lateral keel angles increased, reaching a maximum angle of 54° at the posterior edge of the carapace. The dorsal keel was first noticeable at a location 27% *CL*, forming in the middle of the eye ridge. At this location the dorsal keel was 98°. The dorsal keel generally became sharper posteriorly until approximately 69% *CL*, where the keel angle was 34°. In more posterior regions, the dorsal keel began to broaden again, especially at the posterior edge of the carapace where the keel angle was 108° (Fig. 2).

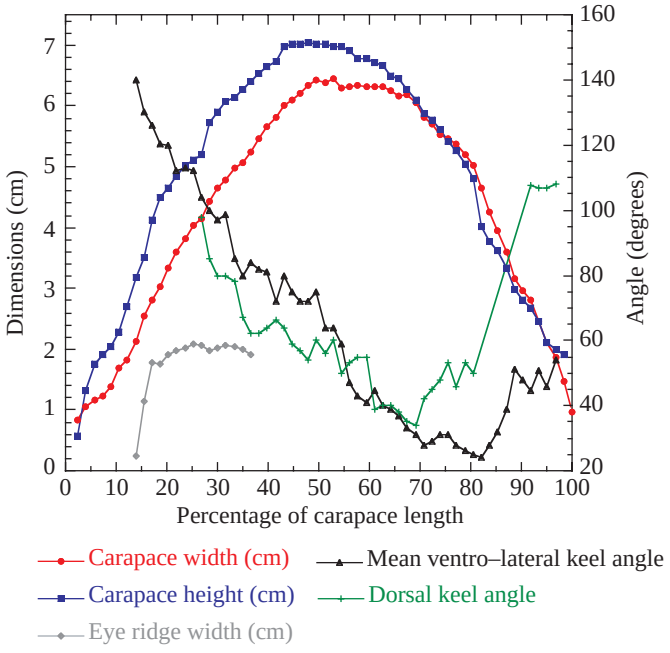

Fig. 2. Characteristics of the carapace of a CT-scanned smooth trunkfish (17.0 cm total length, 12.3 cm carapace length) plotted as a function of percentage of carapace length. Dimensions (carapace width, carapace height, and eye ridge width) are depicted on the left *y*-axis, while mean ventro-lateral keel angle and dorsal keel angle are depicted on the right *y*-axis.

Significant regions of convexity were present laterally along the carapace, especially in areas just posterior to the eye (25–40% *CL*) and near the edge of the carapace (>84% *CL*) (Fig. 3). Along a given dorso-ventral transect, maximum lateral convexity occurred 0.84–2.85 cm below the dorsal keel (Figs 1, 3). Ventral convexity, which was always greatest equidistant from the ventro-lateral keels along transverse transects, actually decreased in magnitude posteriorly until 71% *CL*, at and after which no significant convexity was present (Figs 1, 3). Lateral concavity was present in locations from 38–92% *CL*. Along dorso-ventral transects, maximum lateral concavity occurred 0.38–1.23 cm above the ventro-lateral keels (Figs 1, 3). Ventral concavity was also present in locations from 58 to 94% *CL*. Along dorso-ventral transects, maximum ventral concavity occurred 0.62–1.37 cm from the ventro-lateral keels (Figs 1, 3).

Digital particle image velocimetry

At positive pitching angles of attack, regions of concentrated, discrete vorticity began to develop near the anterior edges of the ventro-lateral keels at a longitudinal location corresponding to the eye ridge (Fig. 4). These regions of concentrated vorticity intensified posteriorly along the ventro-lateral keels, both in terms of peak vorticity and circulation, until two well-developed, counter-rotating vortices ultimately formed at the posterior edge of the carapace. The vortices left the body completely at the caudal peduncle. Some regions of concentrated, attached dorsal vorticity formed along the body as well, especially around the eye ridge, where vortex circulation was stronger dorsally than ventrally at positive angles of attack <20°. However, peak dorsal vorticity and dorsal circulation did not grow steadily along the body, and did not reach the circulation magnitudes observed in ventral areas at the posterior edge of the carapace and at the caudal peduncle. In the wake, dorsal and ventral vortices merged with the vorticity representing the linear lift, producing two well-developed, counter-rotating vortices with a prominent downwash of flow between them (Fig. 4).

At negative pitching angles of attack, regions of concentrated, attached vorticity also began to develop around the ventro-lateral keels at a longitudinal location corresponding to the eye ridge (Fig. 5). As was the case for positive angles of attack, circulation and peak vorticity of ventral vortices increased posteriorly, developing into two counter-rotating vortices at the posterior edge of the carapace, and ultimately

leaving the body completely at the caudal peduncle. However, while regions of concentrated vorticity developed above the ventro-lateral keels at positive pitching angles of attack, regions of concentrated vorticity formed below the ventro-lateral keels at negative pitching angles of attack (Figs 4, 5). Furthermore, vortical flow rotation changed, depending on angle of attack. When viewed from the rear, flow around the right ventro-lateral keel was counterclockwise at positive angles of attack and clockwise at negative angles of attack (Fig. 6). Some regions of weaker, concentrated, attached vorticity formed around the eye ridge in dorsal locations at negative angles of attack, but as was the case at positive angles of attack, the dorsal vortices did not grow steadily along the body like the ventral vortices. In the wake, two well-developed vortices were present with a prominent upwash of flow between them (Fig. 5).

At pitching angles of attack close to 0°, the same general patterns of vortex development occurred: regions of concentrated, attached vorticity formed at the anterior edges of the ventro-lateral keels and grew in terms of peak vorticity and circulation posteriorly, while weaker regions of dorsal vorticity formed sporadically with no consistent antero-posterior circulation growth (Fig. 7). However, circulation and peak vorticity of ventral regions of concentrated, attached vorticity were lower at angles of attack near 0° than at more positive or more negative angles of attack (Figs 6, 7). Irrespective of angle of attack, circulation of attached ventral vortices was always greatest at the posterior edge of the carapace. Interestingly, at an angle of attack of 0°, vortical flow rotation and position resembled conditions at positive angles of attack.

When the carapace was positioned at yawing angles of attack, vortex development occurred adjacent to far-field

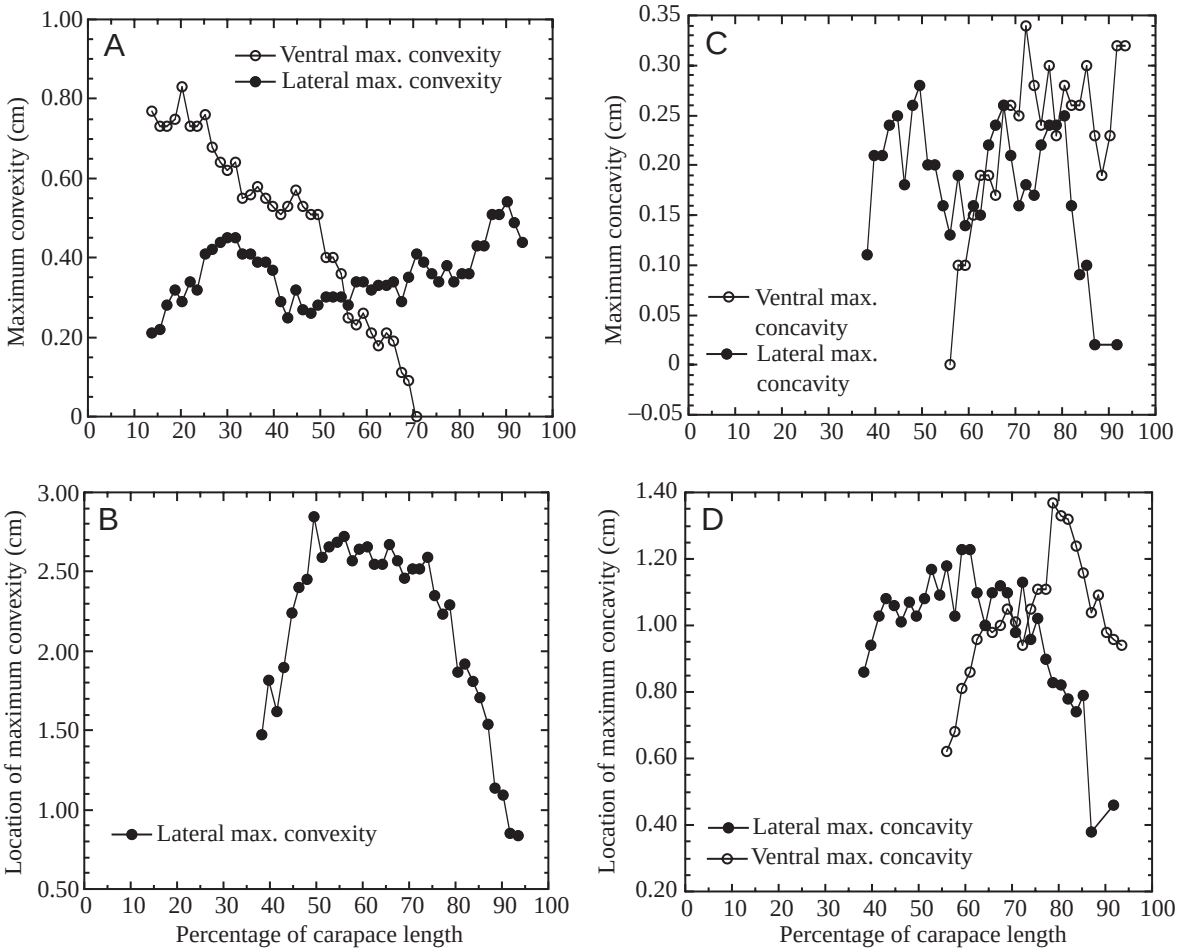

Fig. 3. Concavity and convexity measurements of the carapace of a CT-scanned smooth trunkfish (17.0 cm total length, 12.3 cm carapace length) plotted as a function of percentage of carapace length. Maximum convexity (A) and concavity (C) are the maximum distances that the body extends and indents, respectively, relative to a segment connecting either the tips of the dorsal and ventro-lateral keels (S_L) (lateral measurements) or the tips of the two ventro-lateral keels (S_V) (ventral measurements). The location of maximum lateral convexity (B) is the distance from the dorsal keel to the point of maximum extension along the segment, S_L. The location of maximum lateral/ventral concavity (D) is the distance from the ventro-lateral keel to the point of maximum indentation along segments S_L (lateral) or S_V (ventral). Data on lateral maximum convexity and concavity are mean measurements of the two sides of the carapace. Data on ventral concavity are mean measurements of the two regions of ventral concavity found along S_V. In B the location of ventral maximum convexity occurs equidistant between ventro-lateral keels.

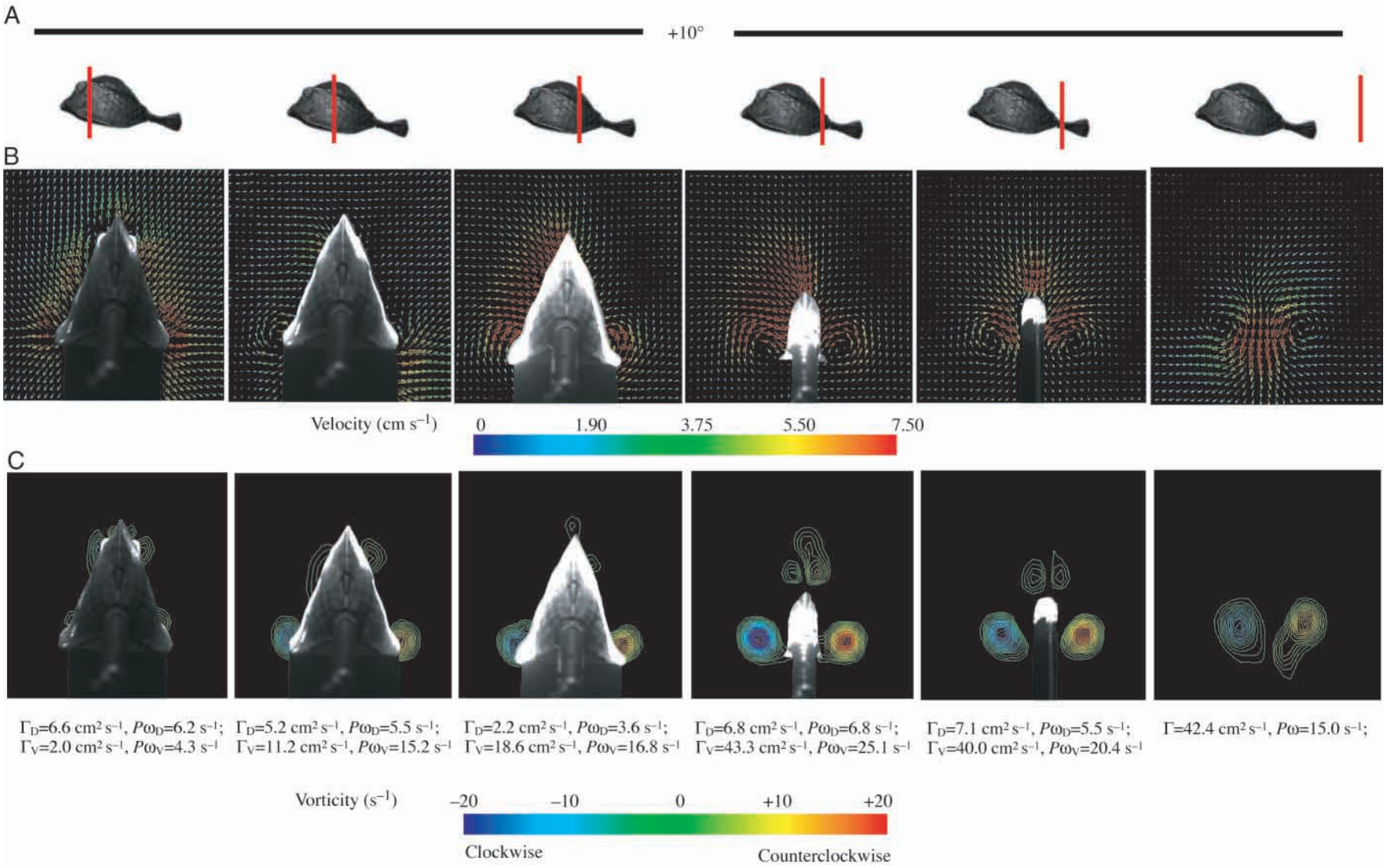

Fig. 4. Velocity vector (B) and vorticity contour (C) fields around and in the wake of the smooth trunkfish model positioned at a pitching angle of attack of +10°. The data are viewed in transverse planes at various locations along the body and in the wake. Each plot is the mean result of 30 velocity fields (1 representative trial). From left to right, the locations (A) are: eye ridge, maximum girth, midpoint between maximum girth and posterior edge of the carapace, posterior edge of the carapace, caudal peduncle and wake. The shadows beneath the models represent areas that were shielded from laser light. Mean circulation magnitude and mean peak vorticity magnitude values for a dorsal vortex (Γ_D and $P\omega_D$, respectively) and a ventral vortex (Γ_V and $P\omega_V$, respectively) are included beneath the vorticity contour plots for measurements along the body. In the wake, dorsal and ventral distinctions are not necessary since ventral and dorsal vortices merge.

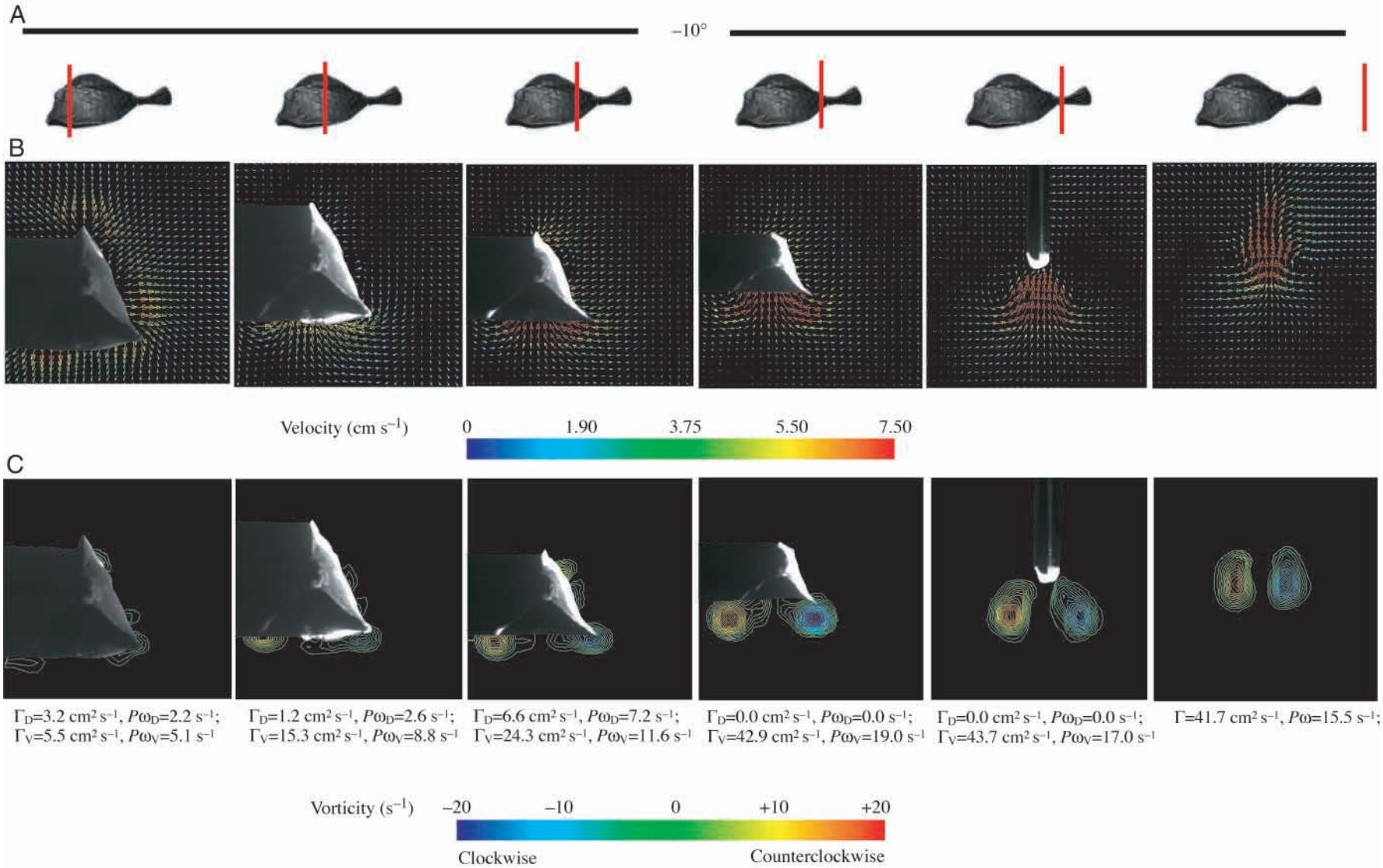

Fig. 5. Velocity vector (B) and vorticity contour (C) fields around and in the wake of the smooth trunkfish model positioned at a pitching angle of attack of –10°. The data are viewed in transverse planes at various locations along the body and in the wake. Each plot is the mean result of 30 velocity fields (1 representative trial). From left to right, the locations (A) are: eye ridge, maximum girth, midpoint between maximum girth and posterior edge of the carapace, posterior edge of the carapace, caudal peduncle and wake. The shadows on the sides of or above models represent areas that were shielded from laser light. Mean circulation magnitude and mean peak vorticity magnitude values for a dorsal vortex (Γ_D and $P\omega_D$, respectively) and a ventral vortex (Γ_V and $P\omega_V$, respectively) are included beneath the vorticity contour plots for measurements along the body. In the wake, dorsal and ventral distinctions are not necessary since ventral and dorsal vortices merge.

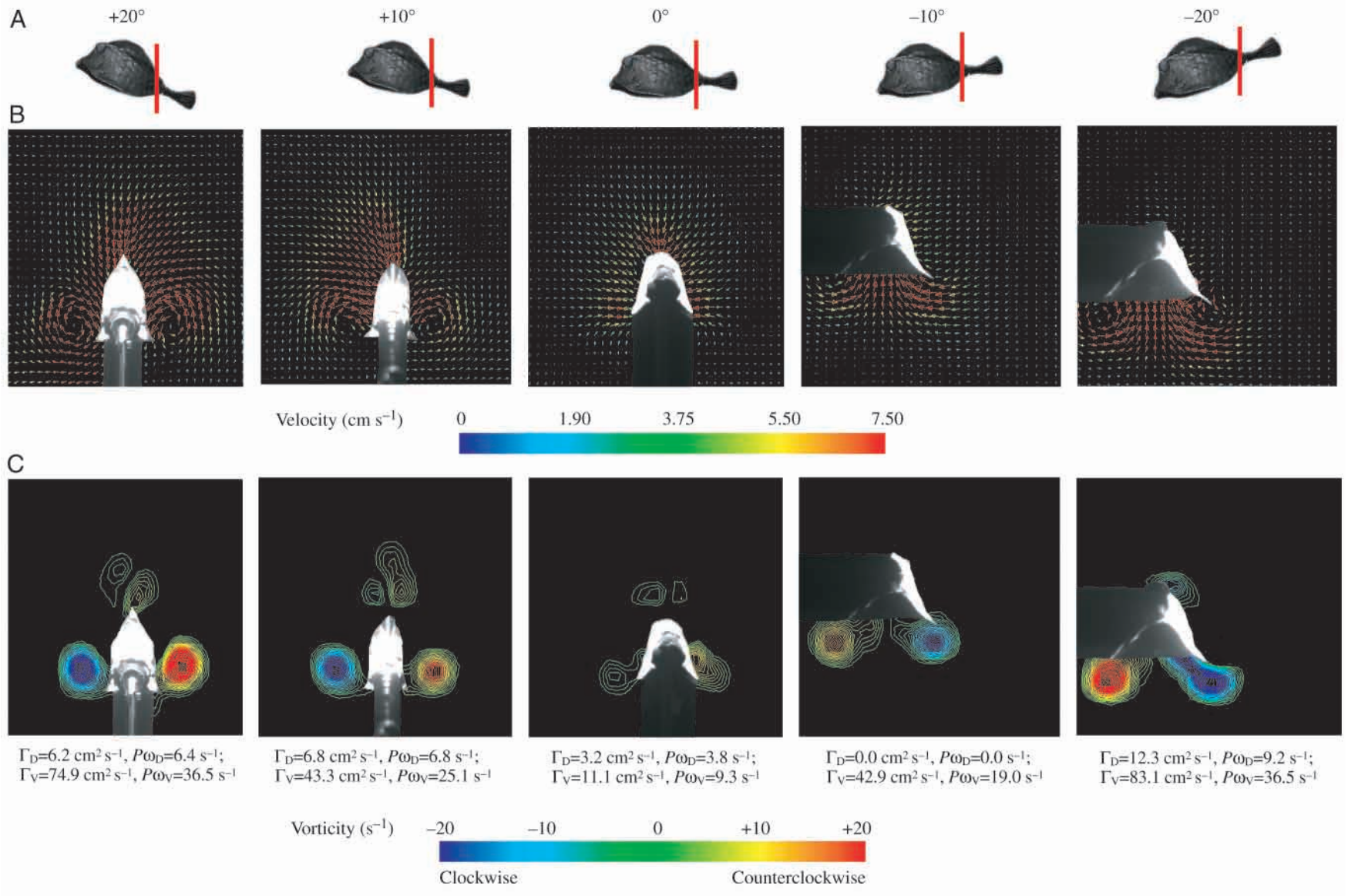

Fig. 6. Velocity vector (B) and vorticity contour (C) fields around the posterior edge of the carapace of the smooth trunkfish model positioned at pitching angles of attack of (left to right): +20°, +10°, 0°, –10° and –20°. The data are viewed in transverse planes, and sampling locations are indicated (A). Each plot is the mean result of 30 velocity fields (1 representative trial). The shadows underneath or to the side of models represent areas that were shielded from laser light. Mean circulation magnitude and mean peak vorticity magnitude values for a dorsal vortex (Γ_D and $P\omega_D$, respectively) and a ventral vortex (Γ_V and $P\omega_V$, respectively) are included beneath the vorticity contour plots.

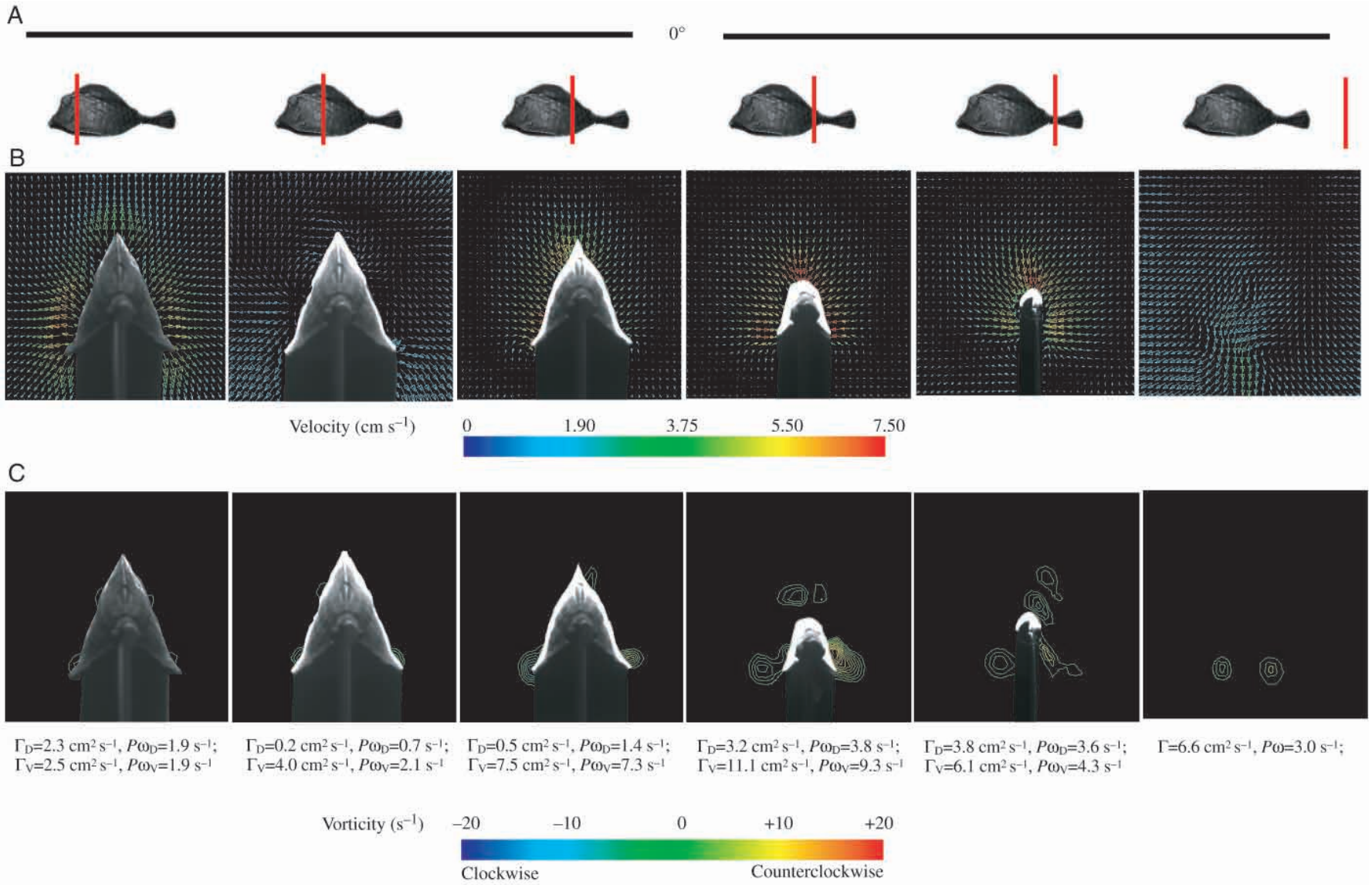

Fig. 7. Velocity vector (B) and vorticity contour (C) fields around and in the wake of the smooth trunkfish model positioned at an angle of attack of 0°. The data are viewed in transverse planes at various locations along the body and in the wake. Each plot is the mean result of 30 velocity fields (1 representative trial). From left to right, the locations (A) are: eye ridge, maximum girth, midpoint between maximum girth and posterior edge of the carapace, posterior edge of the carapace, caudal peduncle and wake. The shadows underneath the model represent areas that were shielded from laser light. Mean circulation magnitude and mean peak vorticity magnitude values for a dorsal vortex (Γ_D and $P\omega_D$, respectively) and a ventral vortex (Γ_V and $P\omega_V$, respectively) are included beneath the vorticity contour plots for measurements along the body. In the wake, dorsal and ventral distinctions are not necessary since ventral and dorsal vortices merge.

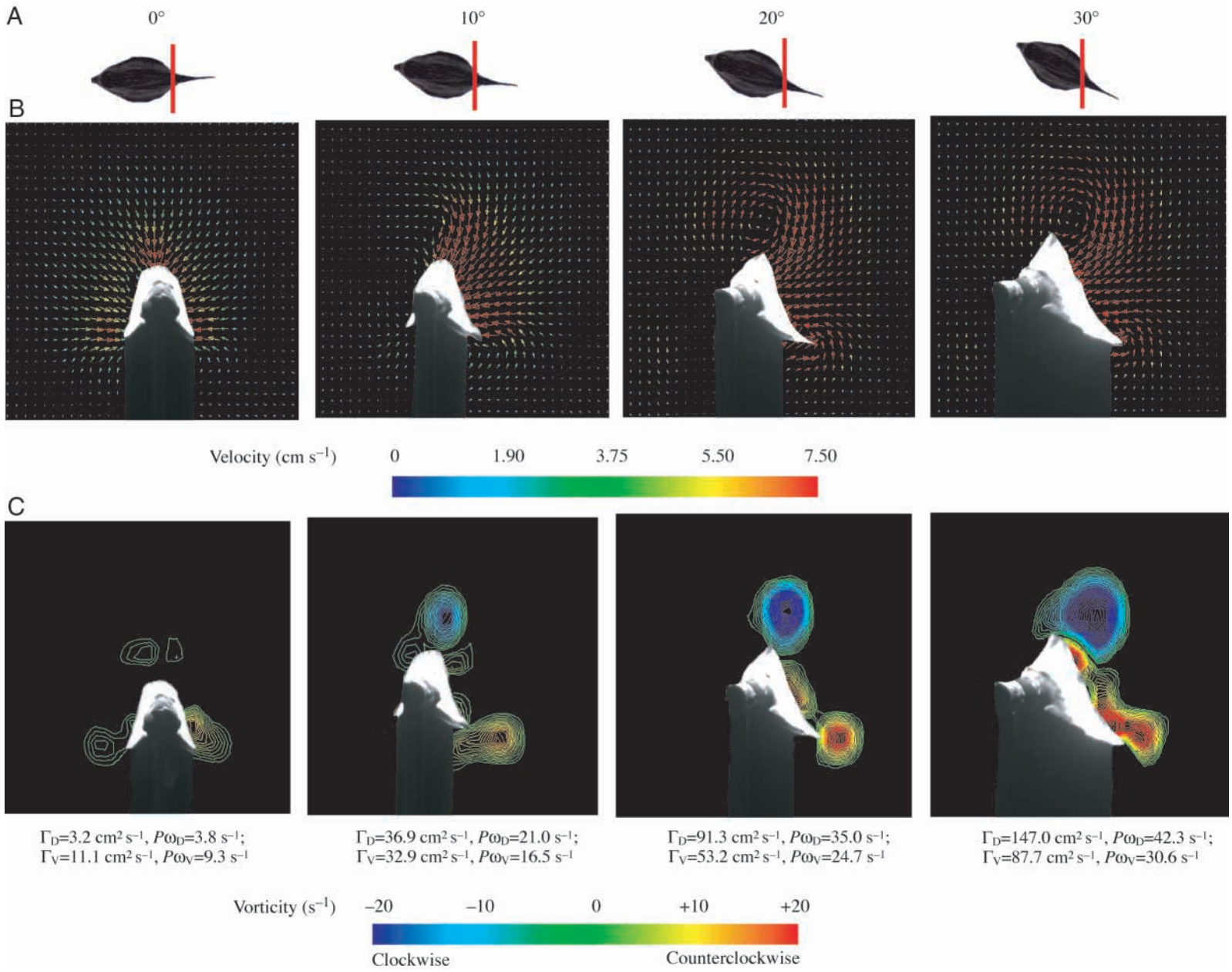

Fig. 8. Velocity vector (B) and vorticity contour (C) fields around the posterior edge of the carapace of the smooth trunkfish model positioned at yawing angles of attack of (left to right): 0°, 10°, 20° and 30°. The data are viewed in transverse planes, and sampling locations are indicated using illustrations of models viewed from above (A). Each plot is the mean result of 30 velocity fields (1 representative trial). The shadows underneath models represent areas that were shielded from laser light. Circulation magnitude and peak vorticity magnitude values for a dorsal vortex (Γ_D and $P\omega_D$, respectively) and a ventral vortex (Γ_V and $P\omega_V$, respectively) are included beneath the vorticity contour plots.

regions of the carapace (i.e. portions of the carapace that are shielded somewhat from oncoming flow), but little concentrated vorticity formed in near-field locations of the carapace (i.e. portions of the carapace that are exposed to oncoming flow) (Fig. 8). At the far-field side of the carapace (the far-field side in this case is the right side of the carapace when viewed from the rear), a clockwise region of concentrated, attached vorticity developed around the eye ridge/anterior edge of the dorsal keel and grew posteriorly in terms of circulation and peak vorticity along the keel. The resulting vortex left the body at either the posterior edge of the carapace or caudal peduncle. One or two counterclockwise regions of concentrated, attached vorticity developed at the anterior edge of the ventro-lateral keel and grew posteriorly along the keel, before leaving the body at either the posterior edge of the carapace or the caudal peduncle. As yawing angles of attack deviated farther from 0°, peak vorticity and circulation of far-field vortices intensified (Fig. 8). As was the case with pitching angles of attack, peak vorticity and circulation of attached vortices were always greatest at the posterior edge of the carapace, irrespective of angle of attack.

Pressure measurements

Locations of the concentrated, attached vorticity observed in DPIV experiments were closely correlated with locations of low pressure detected in pressure experiments. Along the eye ridge dorso-ventral transect, regions of attached vorticity developed around the eye ridge and above the ventro-lateral keel at positive pitching angles of attack. At these locations along the transect, which correspond to pressure ports B4 and B1, respectively, low pressure was also detected (Figs 4, 9). Along the maximum girth dorso-ventral transect, regions of concentrated vorticity were detected laterally and above the ventro-lateral keel, which correspond to pressure ports B7 and

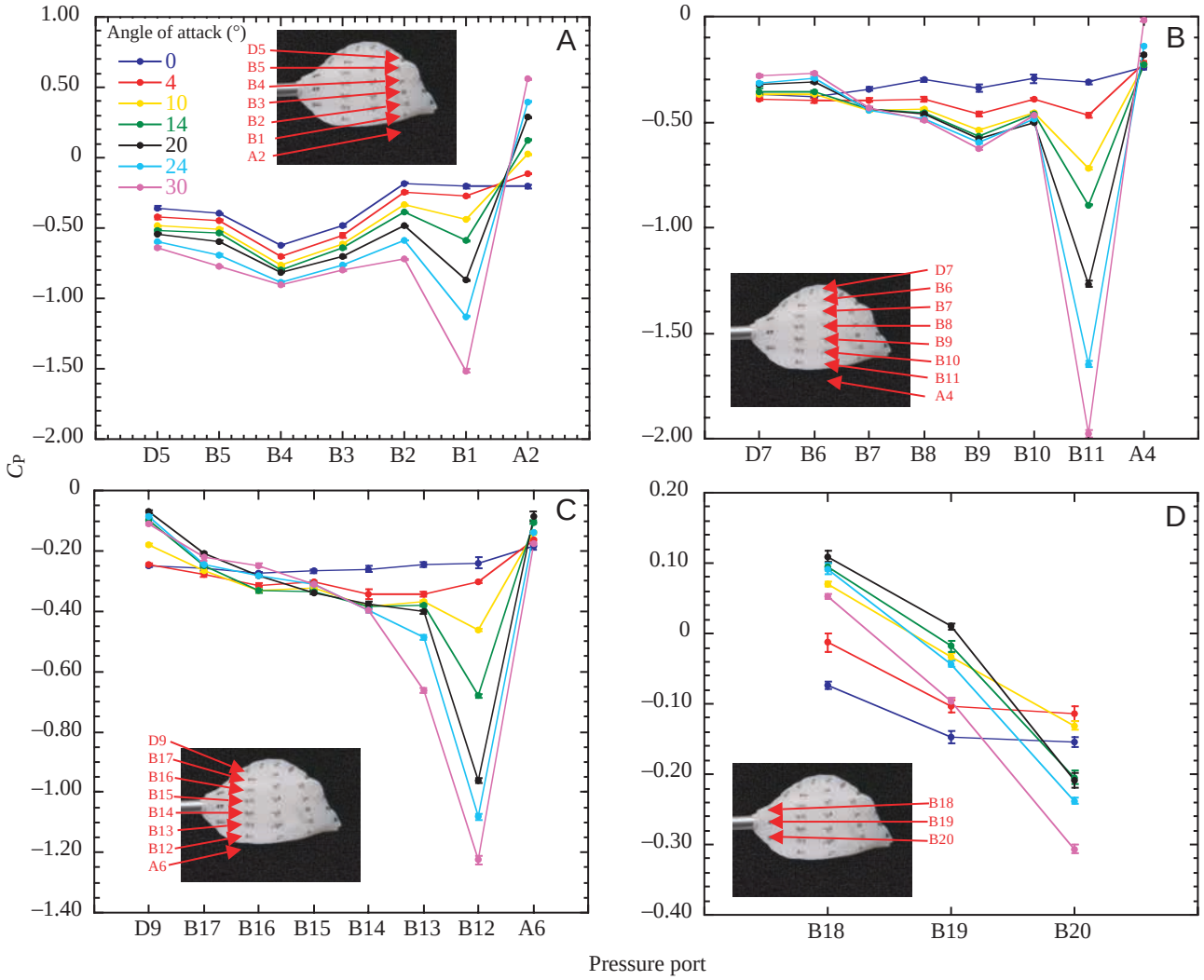

Fig. 9. Pressure coefficients (C_P) plotted as a function of location (pressure port) along various dorso-ventral transects on the smooth trunkfish model positioned at positive pitching angles of attack. The locations of the pressure ports included in each graph are highlighted in images of the model. Note pressure ports A2, A4 and A6 are located in the middle of the ventral region of the carapace, which is not visible in the images. The dorso-ventral transects considered are: (A) eye ridge, (B) maximum girth, (C) midpoint between maximum girth and the posterior edge of the carapace and (D) posterior edge of the carapace. Values are means ± 1 S.D.

B11, respectively. Low pressure at B11 was clearly apparent at all positive pitching angles of attack along the transect. Low pressure at B7 was less apparent, but there was a drop in pressure at B7 relative to its dorsal neighbor B6 at angles of attack >4° (Fig. 9). Along a transect half way between the point of maximum girth and the posterior edge of the carapace, both attached vorticity and low pressure were observed just above the ventro-lateral keel (pressure port B12) at positive pitching angles of attack. At the posterior edge of the carapace, a strong vortex was observed above the ventro-lateral keel at positive pitching angles of attack; at this location (B20 on pressure model) low pressure relative to other points along the dorso-ventral transect was observed. Furthermore, pressure dropped at ports near regions of concentrated, attached vorticity as angles of attack increased, which is consistent with the observed increase in peak vorticity and circulation with higher angles of attack (Fig. 9).

Along the eye ridge dorso-ventral transect, regions of attached vorticity formed around the ventro-lateral keel and the eye ridge at negative pitching angles of attack. Consistent with this observed vorticity pattern, a clear decrease in pressure was observed at B1, a pressure port just above the ventro-lateral keel (Fig. 10). As angles of attack increased, pressure dropped at B1, just as vortex circulation increased at more negative angles of attack. A drop in pressure was also observed at pressure ports near the eye ridge; for angles of attack 0 to –10°, pressure was low at B4, and for angles of attack –20 to –30°, pressure was low at B5. For dorso-ventral transects located at maximum girth and at more posterior locations, regions of concentrated vorticity were located largely just below the ventro-lateral keel at negative angles of attack, an area where no pressure port was located. As a result, there were no consistent declines in pressure at ports just above the ventro-lateral keel (i.e. B11, B12 or B20) along

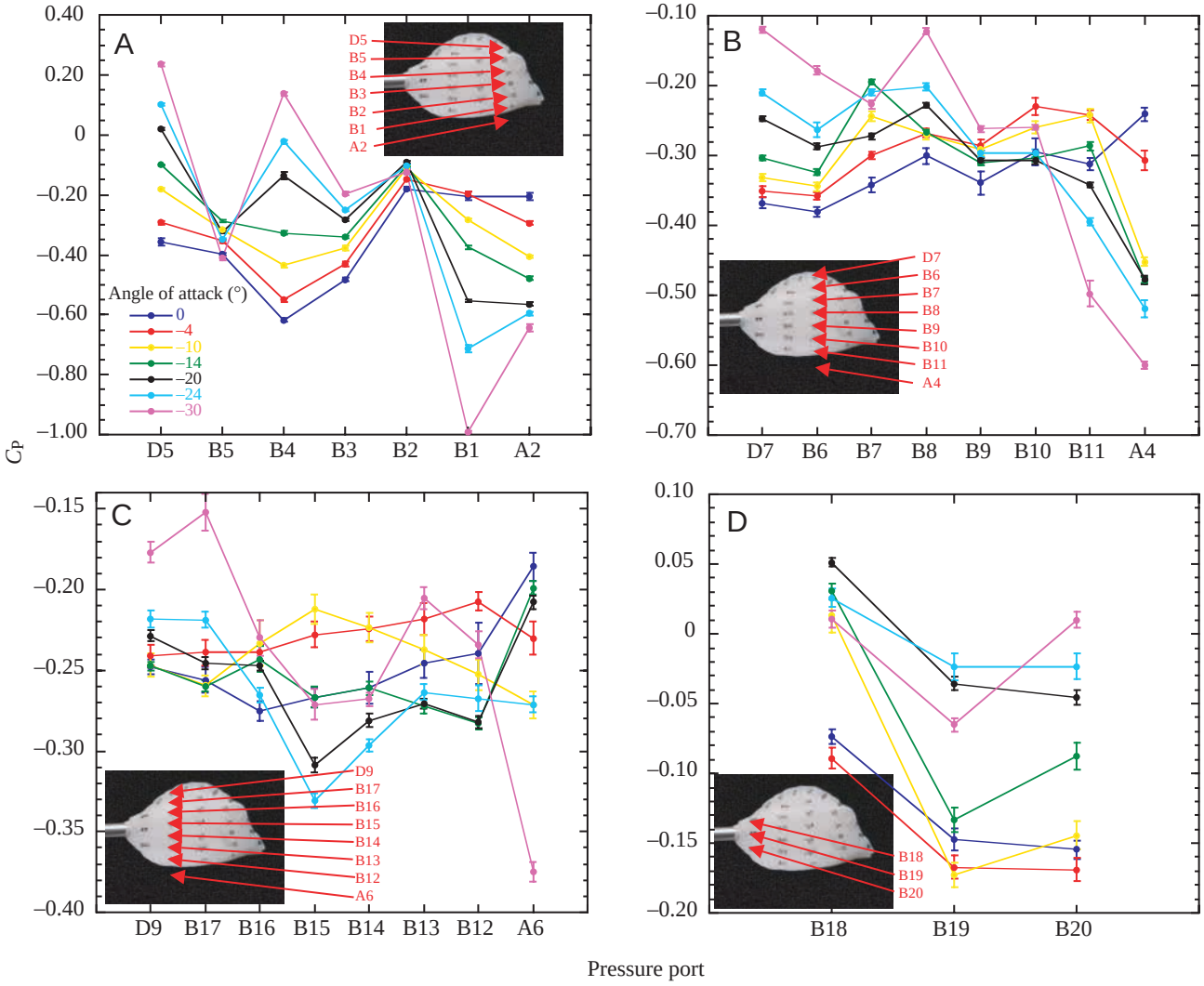

Fig. 10. Pressure coefficients (C_P) plotted as a function of location (pressure port) along various dorso-ventral transects on the smooth trunkfish model positioned at negative pitching angles of attack. The locations of the pressure ports included in each graph are highlighted in images of the model. Note pressure ports A2, A4, and A6 are located in the middle of the ventral region of the carapace, which is not visible in the images. The dorso-ventral transects considered are: (A) eye ridge, (B) maximum girth, (C) midpoint between maximum girth and the posterior edge of the carapace and (D) posterior edge of the carapace. Values are means ± 1 S.D.

dorso-ventral transects as observed at positive angles of attack. Interestingly, at the point of maximum girth, there was a noticeable drop in pressure at A4, a pressure port located in the middle of the ventral region of the carapace that presumably was influenced by regions of ventrally located, concentrated vorticity (Figs 5, 10).

Although peak vorticity and vortex circulation increased consistently along the ventro-lateral keels from the anterior edges of the keels to the posterior edge of the carapace, pressure values did not decrease antero-posteriorly at positive pitching angles of attack. Instead, pressure just above the ventro-lateral keel decreased from the snout to the point of maximum girth (B11), but then increased posteriorly thereafter (Fig. 11). Pressure along the antero-posterior path followed by regions of concentrated ventral vorticity at negative angles of attack was not measured because of a lack of pressure ports. However, along the D1–B20 antero-posterior transect considered for positive angles of attack, pressure was lowest at B1, the only location along the transect where regions of concentrated vorticity were prominent. Along an antero-posterior transect where regions of attached dorsal vorticity were frequently observed, pressure was lowest above and/or behind the eye ridge (D4, B5) at both positive and negative angles of attack (Fig. 11), areas where regions of concentrated, attached dorsal vorticity were frequently greatest. Dorsal pressures at positive angles of attack were lower than at negative angles of attack, which too is consistent with the observed vorticity patterns, i.e. there was stronger concentrated vorticity around the eye ridge at positive as opposed to negative angles of attack.

At yawing angles of attack, vortex formation occurred at the far-field side of the carapace, most prominently in regions adjacent to the dorsal and ventro-lateral keels. Low pressure was consistently detected in these regions along dorso-ventral transects. For example, at the point of maximum girth, pressure at D7 (port just below dorsal keel) and B11 (port just above

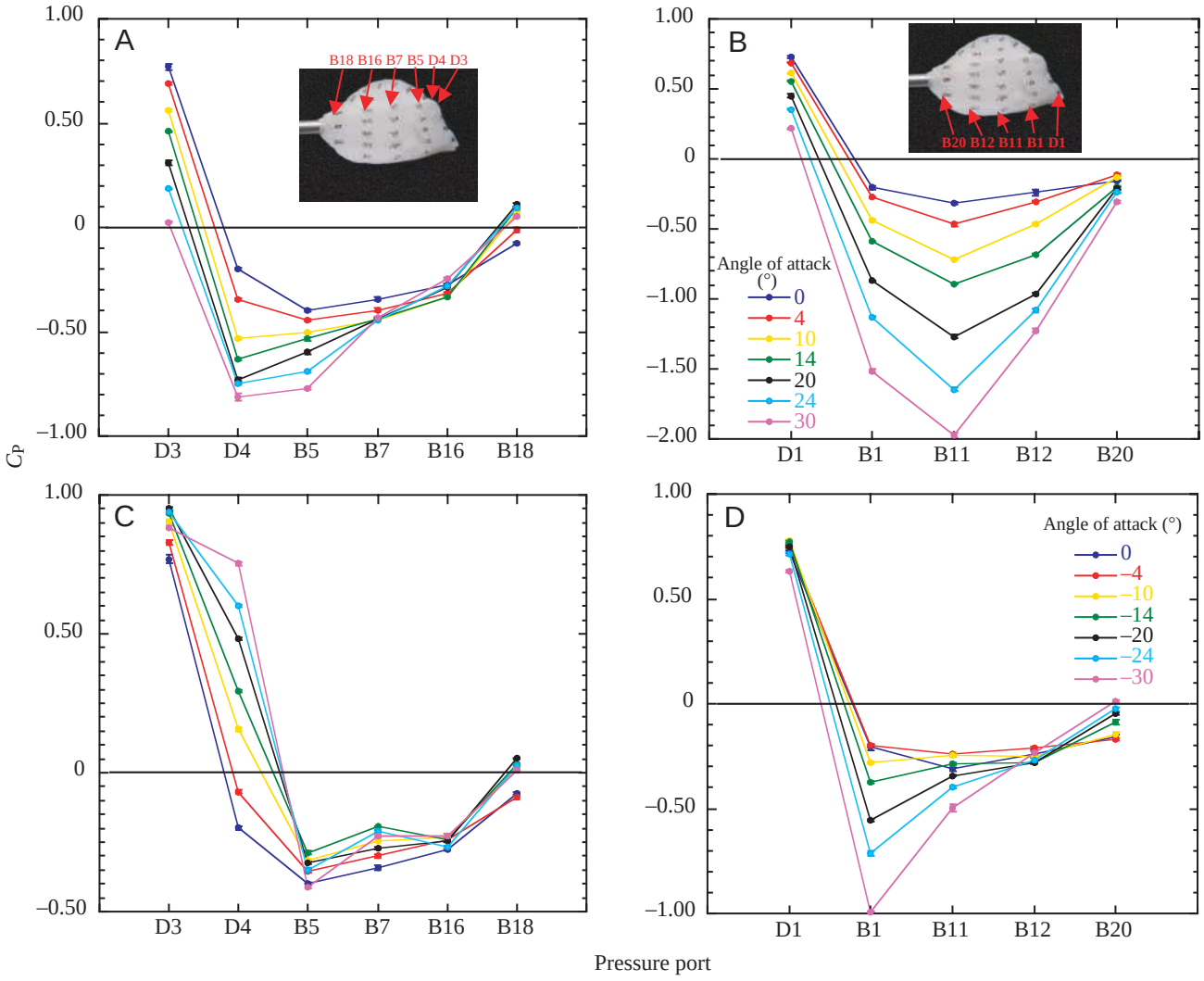

Fig. 11. Pressure coefficients (C_P) plotted as a function of location (pressure port) along dorsal antero-posterior transects (A,C) and ventral antero-posterior transects (B,D) on the smooth trunkfish model positioned at different pitching angles of attack. Positive pitching angles of attack are depicted in A and B, while negative pitching angles of attack are depicted in C and D. The locations of the pressure ports included in each graph are highlighted in images of the model in A and B. Values are means ± 1 S.D.

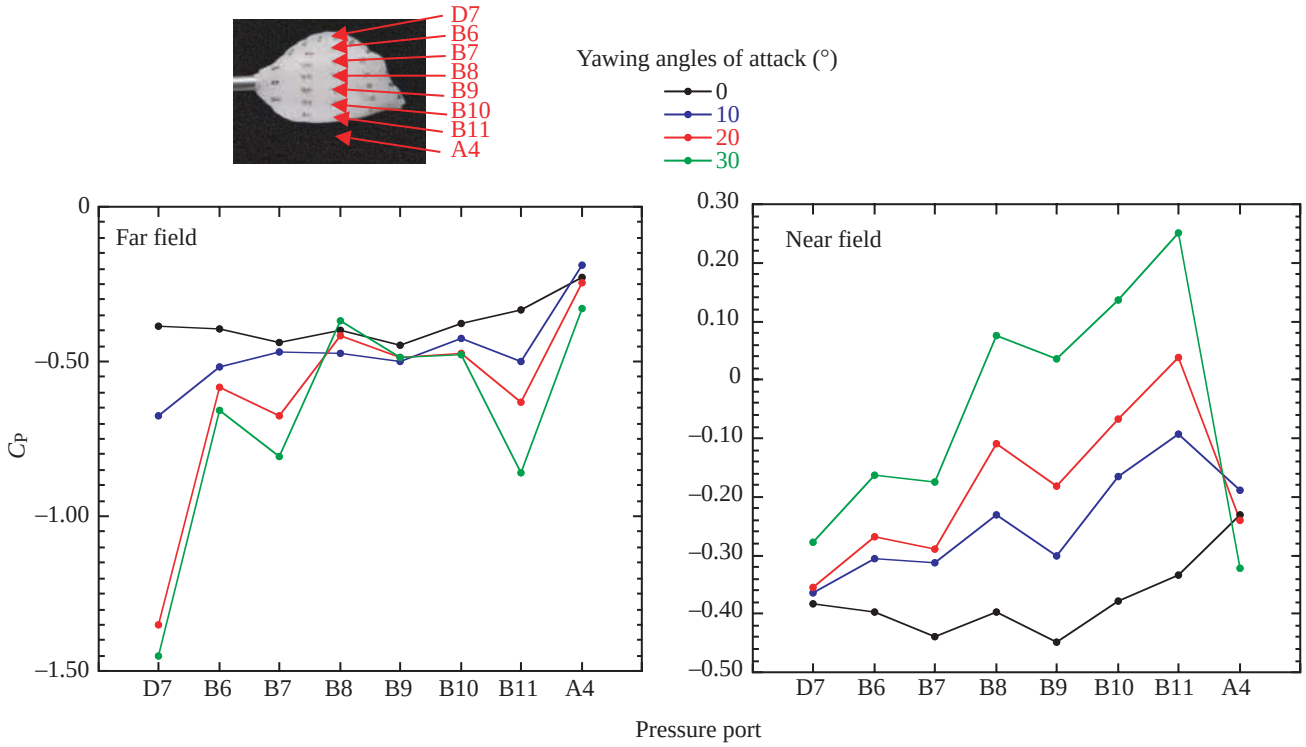

Fig. 12. Pressure coefficients (C_P) plotted as a function of location (pressure port) along a dorso-ventral transect at the maximum girth point of a smooth trunkfish model positioned at different yawing angles of attack. The graph on the left depicts conditions when the transect is in the far field, i.e. shielded from flow, whereas the graph on the right depicts conditions when the transect is in the near field, i.e. exposed to flow. The locations of the pressure ports included in each graph are highlighted in the image of the model. A4 is located in the middle of the ventral region of the carapace.

ventro-lateral keel) was low when models were positioned at yawing angles of attack with the ports in the far field (Fig. 12). Moreover, a clear drop in pressure at lateral locations between the dorsal and ventro-lateral keel (i.e. B7–B9) was frequently observed, which is where additional regions of concentrated vorticity were detected using DPIV (Figs 8, 12). As circulation and peak vorticity increased with increasing yawing angle of attack, pressure in regions of concentrated vorticity dropped. When the model was positioned so that the holes were in the near field, i.e. directly exposed to flows, a very different pressure distribution occurred. As the pressure ports were exposed to a larger normal velocity component in the near-field side (i.e. higher angles), pressure actually rose at all the lateral ports (Fig. 12).

Force balance measurements

No obvious stall occurred at angles of attack up to ±30°, and overall lift coefficients of the carapace were similar to coefficients of delta wings of similar aspect ratio (Fig. 13). The lift coefficient of the carapace was closest to 0 at –2° (C_L=–0.005). At 0°, C_L was 0.027. The drag coefficient of the carapace was lowest at –4° (C_D=0.157) and was 0.167 at 0°. At positive angles of attack, the lift-to-drag ratio was highest at +20°, which is consistent with delta wings that often have maximum L/D ratios >15° (Bertin and Smith, 1989). At negative angles of attack, the highest downward-directed lift to drag ratio occurred at –16°. Nose-down pitching moments about the center of mass were detected at angles of attack >–2°, while nose-up pitching moments about the center of mass were detected at angles of attack <–2° (Fig. 13).

When compared to lift measurements from force balance experiments, lift values predicted from DPIV circulation values (using 2-D airfoil equations) were consistently of higher magnitude (paired sample *t*-test, mean difference=0.045, d.f.=6, *t*-value=4.322, *P*=0.005). At positive angles of attack, DPIV lift estimates were 29–33% higher in the positive direction than force balance lift measurements. At negative angles of attack, DPIV lift estimates were 25–38% higher in the negative direction than force balance lift measurements (Fig. 14).

Discussion

This study is the first to our knowledge that applies multiple aerodynamic and hydrodynamic engineering methods to address an important question in the functional morphology of fish locomotion, i.e. what are the physical bases for the exceptional hydrodynamic stability of swimming found in the ostraciid fishes? The results demonstrate that: (1) it is possible to obtain internally consistent, independent lines of data that collectively address the question; and (2) morphological features of the carapace contribute to hydrodynamically stable swimming. This paper establishes the foundations for a larger,

similar, comparative study of carapace morphologies and fluid flow properties for each of the major variations in body form that occur in the ostraciids. Those results will be presented in another paper.

Morphological features

The results of this study indicate that prominent vortices form along the body when smooth trunkfish *L. triqueter* pitch and yaw. The morphological features of the carapace play an instrumental role in the generation, growth and persistence of these vortices. The anterior origins of the ventro-lateral keels, which were present at locations approximately 14% *CL*, force flow separation and the generation of vorticity during pitching and yawing. The ventro-lateral keels extend along the majority of the length of the carapace, becoming sharper posteriorly up to a location 82% *CL* and providing a large area for vorticity buildup along the body. These characteristics facilitate vortex circulation growth in areas adjacent to the ventro-lateral keels. Regions of lateral concavity found 38–92% *CL* and 0.38–1.23 cm above the ventro-lateral keels and ventral concavity present 58–94% *CL* and 0.62–1.37 cm below the ventro-lateral keels provide channels for vortices to develop, and serve to fix developing vortices in place at various pitching and yawing angles of attack. The steep lateral sides and prominent dorsal ridge also play important roles in isolating developing ventro-lateral flows, allowing counter-rotating vortices to form without interaction with one another. The eye ridge, which was consistent in width and present at 14–37% *CL*, and dorsal keel, which became sharper posteriorly up until approximately 70% *CL*, are responsible for forcing flow separation and the generation of vorticity in dorsal regions when smooth trunkfish pitch and yaw, respectively. During yawing, vortex circulation growth along the carapace is facilitated by the dorsal keel when one side of the keel is exposed to larger normal velocity components than the other. However, during pitching, the lack of multiple, laterally extended dorsal keels, which would allow the two regions of vorticity shed from the eye ridge to grow in strength posteriorly with minimal interaction with one another (as in ventral regions), inhibits vortex circulation growth along the carapace. Consequently, vortex circulation in posterior regions of the carapace is weaker dorsally than ventrally during pitching.

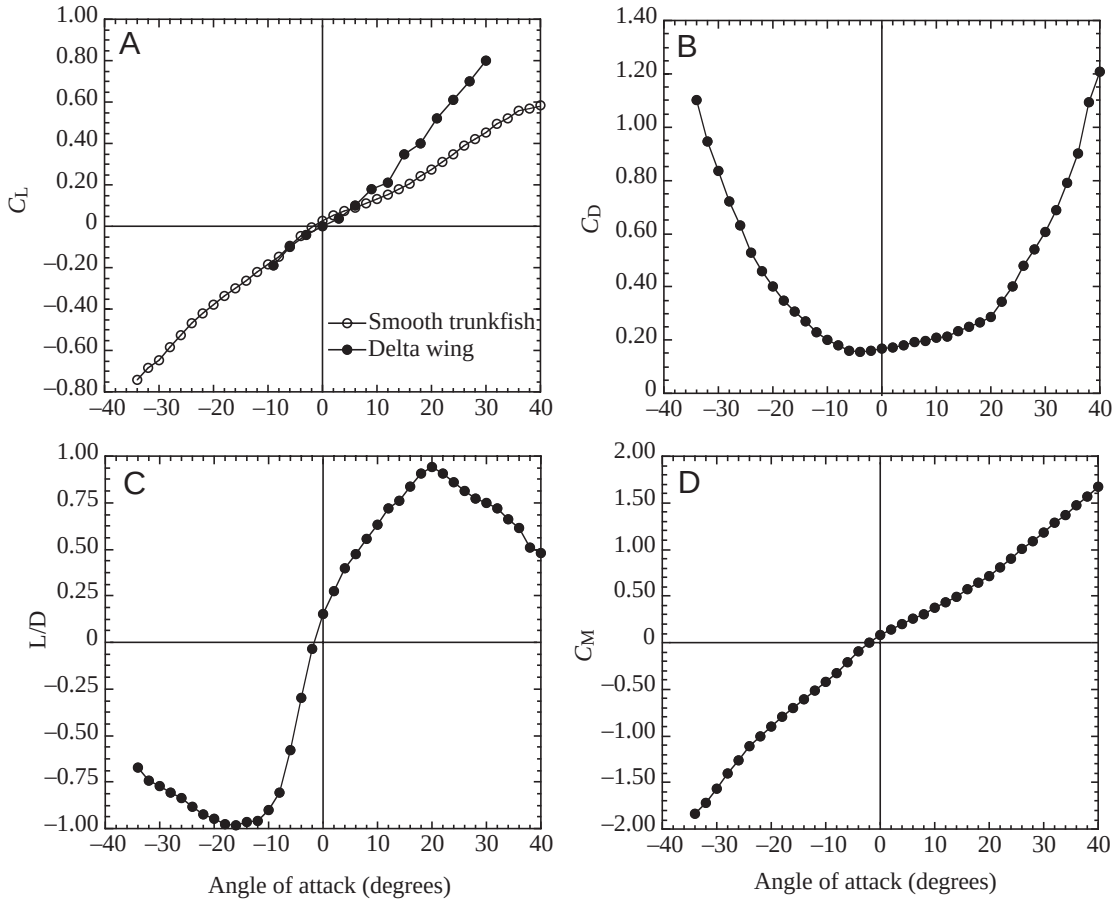

Fig. 13. Lift coefficients (C_L; A), drag coefficients (C_D; B), lift to drag ratios (L/D; C), and pitching moment coefficients about the center of mass (C_M; D) for the smooth trunkfish model positioned at various pitching angles of attack. In the lift coefficient plot (A), smooth trunkfish coefficients are depicted as open circles, while delta wing coefficients are depicted as filled circles. The delta wing has a similar aspect ratio (0.83) to that of the smooth trunkfish. Delta wing data are from Schlichting and Truckenbrodt (1969). Positive pitching moment coefficients (D) indicate a nose-down pitching moment about the center of mass, whereas negative pitching coefficients indicate a nose-up pitching moment about the center of mass.

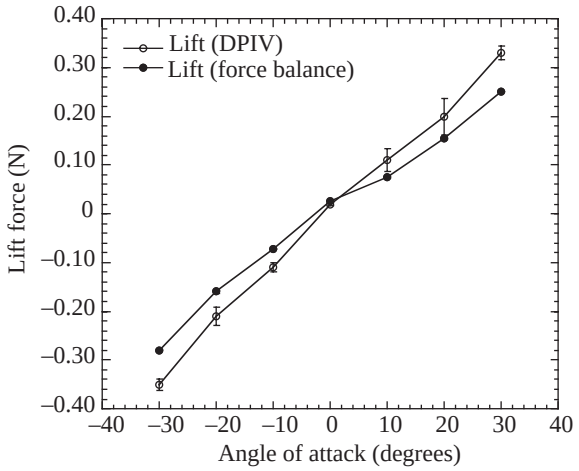

Fig. 14. Lift forces acting on a smooth trunkfish model measured using a force balance (filled circles) and DPIV (open circles) plotted as a function of angle of attack. Values are means ± 1 S.D. In the force balance measurements, S.D. bars are often smaller than the symbols used to denote values.

Self-correction for pitching

DPIV measurements, which provide a global picture of flow around the body within planar domains, indicate that pitching angle of attack has a large impact on ventral vortex formation. As angles of attack increased from approximately 0° in the positive direction, vortices with stronger peak vorticity and circulation developed along concavities above ventro-lateral keels, beginning at the anterior origins of the ventro-lateral keels and reaching maximum strength at postero-lateral regions of the carapace. As angles of attack increased from approximatey 0° in the negative direction, vortices with stronger peak vorticity and circulation developed along ventral concavities below the ventro-lateral keels, beginning again at the anterior origins of the ventro-lateral keels and reaching maximum strength at postero-ventral regions of the carapace. At angles near 0°, weak vortices with the lowest circulation developed along the ventro-lateral keels.

Pressure measurements, which provide useful information on flow conditions at the surface of the carapace, an area difficult to resolve with DPIV because large velocity gradients within the boundary layer require high particle densities and small interrogations windows to resolve, were consistent with the global flow patterns. In regions where attached, concentrated vorticity was observed, areas of low pressure were consistently detected on the carapace surface. Moreover, as angles of attack deviated farther from 0°, either in a positive or negative direction, and circulation of attached vortices increased, pressure dropped accordingly. These correlations are in agreement with Bernoulli's Law, which states that higher local speeds result in lower static pressure. Near the core of each vortex, flow speeds are higher than the surrounding fluid and consequently static pressure is low. As the vortex intensifies in strength and local speeds increase, pressure becomes more negative (McCormack and Crane, 1973; Tritton, 1998; Vogel, 1994). Consequently, for those ports located near the vortex core, a low-pressure region is detected and becomes more conspicuous as angles of attack increase. Along some dorso-ventral transects, a high-pressure region adjacent to the low-pressure vortex core region was present (e.g. B2 and B10 in Fig. 9). This high-pressure region is indicative of a slow flow area where separated flow comes to reattachment, a process that is visible in the velocity vector and vorticity contour fields for the respective transects (Fig. 4). The farther the vortex core migrates from the carapace surface, the less effect it has on pressure at the surface because the induced velocity drops with growing distance. This point is illustrated by the observed increase in pressure along an antero-posterior transect above the ventro-lateral keel, beginning at maximum girth and progressing posteriorly to the edge of the carapace. Despite an observed increase in vortex circulation along the antero-posterior transect, localized surface pressures did not continue to decrease along the transect because the vortex core migrated away from the carapace, thus having less effect on surface pressure (see Figs 4, 11). This result highlights the importance of using pressure and DPIV data in conjunction; linking global flow features with their concomitant localized effects on the smooth trunkfish carapace is critical for fully understanding flow effects.

Force measurements, which afford an integrative view of the forces acting on the entire carapace, provide further support for the flow patterns detected in DPIV and pressure experiments. Based on DPIV and pressure results, vortices are generated near the anterior of the fish and grow in strength as they move posteriorly down the carapace, most prominently in regions adjacent to ventro-lateral keels. Delta wings, which have comparable planforms to smooth trunkfish, produce similar flows. In delta wings, a coiled vortex sheet with a core of high vorticity forms at the leading edge of the wing and grows posteriorly along the wing generating lift – a process that differs from lift created through bound circulation in conventional wings and leads to higher angles of attack for stall (Bertin and Smith, 1989). The observed similarity in lift coefficients and L/D ratios between delta wings and smooth trunkfish is thus further evidence of vortex generation and subsequent growth along the ventro-lateral keels. Based on force measurements, lift coefficients were closest to 0 at –2° and were slightly positive at 0°. This too is in agreement with DPIV data. DPIV results indicate that lowest vortex circulation occurs at angles of attack near 0°, and vortices are generated above ventro-lateral keels at 0°, providing beneficial lift for counteracting negative buoyancy present in rigid-bodied ostraciids (Blake, 1977).

The vortical flow patterns summarized here produce trimming forces that self-correct for pitching motions, i.e. rotation in the vertical, head up/down longitudinal plane. Attached vortices with the strongest peak vorticity and circulation generally develop posterior to the center of mass; the center of mass of smooth trunkfish is located at a longitudinal location corresponding approximately to the point of maximum girth (Bartol et al., in press). These vortices form

above (positive angles of attack) or below (negative angles of attack) ventro-lateral keels that extend laterally at an angle of 25–40° relative to a horizontal axis when viewed in cross section. Consequently, suction derived from the presence of a vortex above or below the ventro-lateral keels, which was evident as low pressure zones in pressure experiments, should act largely upward and posterior to the center of mass at positive angles of attack (which also occurs in delta wings) and downward and posterior to the center of mass at negative angles of attack. Based on pitching moments recorded in force balance measurements, where nose-down pitching moments occurred and became progressively stronger as angles of attack became more positive, and nose-up pitching moments occurred and became progressively stronger as angles of attack became more negative, this is exactly what happens. Therefore, the ventro-lateral keels are effectively generating self-correcting forces for pitching motions; the self-correcting couple is proportional to the angle to which the fish is perturbed from a horizontal swimming trajectory.

Dorsal and antero-posterior flows

Regions of attached, concentrated vorticity detected around the dorsal eye ridge in this study did not grow in a uniform manner antero-posteriorly during pitching, as was the case for ventral keel induced vorticity. Instead regions of concentrated dorsal vorticity largely broke down along the body posterior to the eye ridge, irrespective of pitching angle of attack. These results again are consistent with the observed pressure distributions. If dorsal carapace morphology does not facilitate the growth of vortices posteriorly, is there an advantage to producing vorticity and creating the observed pressure distributions at the eye ridge, i.e. is there a hydrodynamic purpose of the eye ridge? Given that ambient pressure occurs around the eye ridge regardless of angle of attack, the eye ridge may generate the observed flows to ensure an optimal pressure distribution around the eye. Maintaining ambient pressure around the eye is advantageous because the eye (and most importantly the lens) will not be pushed in or pulled out as flow moves along the body, which improves eye function. Detection of ambient pressures around the eyes has been reported in other nekton, such as squid, bluefish, and tuna (Aleyev, 1977; Dubois et al., 1974; Vogel, 1987). In addition to creating an optimal pressure distribution around the eye, the eye ridge may generate some lift to counteract the nose-down pitching moment produced by the ventro-lateral keels at a 0° angle of attack, thus allowing for more uniform lift generation about the center of mass to counteract negative buoyancy. This proposed function is analogous to the role of canards on delta wing aircraft, which provide nose-up trimming moment to counteract nose-down pitching (Bertin and Smith, 1989).

Based on pressure distributions along antero-posterior transects, there is no appreciable flow separation from the posterior edge of the carapace in ventro-lateral regions (i.e. pressure coefficients are not greater than ambient pressure (C_P=0) and pressure gradients are gradual). Flow remains bound to the carapace, presumably because of the ventral vortices, which pick up vorticity and energize flow close to the carapace surface. Based on the observed positive pressure coefficients at the posterior edge of the carapace in dorsal locations, flow separation appears to occur in dorsal, posterior regions of the carapace for angles of attack >4°. According to pressure distribution measurements of other aquatic organisms, flow separation occurs near the eye and anterior to the arms of squid *Loligo pealei* swimming tail-first (Vogel, 1987), at the posterior quarter of the body of penguins *Pygoscelis papua*, *P. aseliae* and *P. antartica* and tuna *Trachurus mediterraneus* (Aleyev, 1977; Bannasch, 2000), and at the posterior half of the body of a swordfish *Xiphias gladius* (Aleyev, 1977). Using surgically implanted catheters, Dubois et al. (1974) found that flow does not separate anterior to the caudal peduncle in bluefish *Pomatomus saltatrix*. Results from both Dubois et al. (1974) and the present study are significant because they suggest that fin motion may not be necessary to keep flow attached to the body, as suggested in other studies (Aleyev, 1977; Blake, 1983b).

Self-correction for yawing

The flow patterns and pressure distributions detected around and along the carapace at various yawing angles of attack indicate that the carapace also generates self-correcting forces for yawing, i.e. rotations in the left/right horizontal frontal plane. Dorsal and ventral vortices clearly formed on the far-field side of carapace, especially in areas adjacent to the dorsal and ventro-lateral keels, when the smooth trunkfish model was positioned at various yawing angles of attack. Circulation of attached vortices increased posteriorly along the carapace, such that maximum vortex circulation occurred posterior to the center of mass. Vortex circulation and peak vorticity also increased as yawing angles increased. In areas where concentrated attached vorticity was observed, low pressure was detected, and as circulation of attached vortices increased with increasing angle of attack, pressure dropped accordingly. Suction derived from the presence of vortices at far-field locations of the carapace acts largely opposite the direction of the yaw and posterior to the center of mass, thus providing trimming forces that self-correct for yawing motions. As with pitching, the self-correcting couple is proportional to the angle to which the fish is perturbed.

Hydrodynamic stability in boxfishes

Hove et al. (2001) found that boxfishes exhibit some of the smallest amplitude recoil moments known among fishes. As a result, they swim in smoother trajectories than either body- and caudal-fin (BCF) or single-complex median- and paired-fin (MPF) swimmers. Results from the three independent but complementary experimental approaches applied in this study indicate that the keeled bony carapace plays an important role in producing both longitudinal and latitudinal stability in at least one species of boxfish, the smooth trunkfish *L. triqueter*. In addition to producing self-correcting forces, the bony carapace of the smooth trunkfish also appears to incur high drag; the drag coefficients reported in this study are higher than

those typically recorded in other fish, by as much as an order of magnitude (Blake, 1981, 1983a). Given that Anderson et al. (2001) found that live, flexible-bodied swimming fish have much greater friction drag than has been reported in the literature because of boundary layer thinning and streamwise acceleration of the near-field, drag differences between boxfish and flexible-bodied fish may be less pronounced than expected. Nonetheless, control for pitching and yawing is presumably more important than drag reduction for fishes like smooth trunkfish. These fishes generally move relatively slowly, but live in highly energetic waters with frequent external disturbances, like turbulence, that can lead to large displacements and significant energy-wasting trajectories. The trimming self-corrective forces produced by the carapace limit these displacements and are especially advantageous for the unpredictable velocity fields experienced by smooth trunkfish because rapid neural processing – a factor that may limit correction responses to sudden, erratic perturbations – is not required, as in powered control systems (Webb, 2000). In addition to the energy savings associated with self-correction for disturbances, maintenance of smooth swimming trajectories also presumably improves sensory acuity of both hostile and target objects because it reduces complexity of movement, a factor that improves sensory perception in other animals (Land, 1999; Kramer and McLaughlin, 2001).

Trimming and powered forces provided by the fins also presumably play an important role in the control and regulation of trajectories. Like spotted boxfish, smooth trunkfish have four low aspect-ratio median and paired fins of nearly identical area that assuredly move in complex ways together with the caudal fin to minimize recoil motions (Hove et al., 2001; I. Bartol, unpublished morphological measurements of smooth trunkfish). The pectoral fins, in particular, may play an important role in the structure of vortices forming along the ventro-lateral keels since the pectoral fins are located near the path of body-induced vortex formation. Studies focusing on the interactions between flows over the fins and over the bodies of live boxfishes are underway in our laboratories. Although fin flow and body flow interactions are present in live fishes, the results of this study are applicable to freely swimming fishes because the underlying physical functioning of the carapace self-correcting system is not affected by fin/body flow interactions. When angles of attack deviate from 0° in either the positive or negative direction, vortex strength increases along the carapace. The self-correcting effect of these vortices will still occur, irrespective of whether vortex strength increases relative to magnitudes measured for the body alone, or for some fin-modified value.

Quantifying and visualizing flow patterns around oscillating fins poses a significant challenge for understanding stability in smooth trunkfish. DPIV is a powerful tool that has been applied to a number of interesting areas of fish locomotion, ranging from wakes around flexing bodies (Stamhuis and Videler, 1995; Wolfgang et al., 1999; Müller et al., 2001), fin function (Drucker and Lauder, 1999, 2000, 2001a; Wilga and Lauder, 1999, 2000), fluid forces during turning maneuvers (Wolfgang et al., 1999; Drucker and Lauder, 2001b), flows around the caudal peduncle and finlets (Nauen and Lauder, 2001), vorticity control in fish-like propulsion (Beal et al., 2001), and boundary layer flows (Anderson et al., 2001). However, DPIV has one significant limitation: it is a 2-D measurement platform that does not consider all three flow-field components, which may ultimately lead to some error when calculating propulsive and resistive forces. An example of such error was encountered in the present study. Lift forces determined using DPIV were consistently higher than those measured directly using a force balance. A comparable situation was also detected by Noca et al. (1997) when measuring instantaneous forces on a cylinder in an incompressible cross-flow. These errors occurred because a 2-D rather than a 3-D velocity field was used to determine force.

Future studies on live smooth trunkfish will be performed using defocusing digital particle image velocimetry (DDPIV), a new method that allows us to visualize and quantify flows in three dimensions as they move along the body and around the fins (Pereira et al., 2000; Pereira and Gharib, 2002). Since this technique allows for the quantification of flows over a significant volume of fluid, it is an improvement on, not only current 2-D DPIV systems, but also stereo-DPIV technology, where 3-D flows are imaged in a thin slice of fluid. Employing DDPIV technology to study stability in live rigid-bodied boxfishes promises to provide unprecedented information on the control and regulation of trajectories in rigid-bodied multi-propulsor swimmers.

List of symbols

A_f	maximum frontal area
A_p	planform surface area of the ventral region of the carapace
BL	body length of fish
c	chord length of carapace
C_D	drag coefficient
CL	carapace length of fish
C_L	lift coefficient
C_M	pitching moment coefficient
C_P	pressure coefficient
D	total drag
d_1	distance between load cell beams in the force balance
d_2	distance between center of force balance and center of mass of model
DPIV	Digital particle image velocimetry
L	total lift
L_1	lift measured at load cell closest to model
L_2	lift measured at load cell farthest from model
L_s	lift per unit span
M	pitching moment
S_L	segment connecting the apices of ventro-lateral and dorsal keels
S_V	segment connecting the apices of the two ventro-lateral keels
TL	total length of the fish
u	flow speed

U wind speed
α angle of attack
Γ mean vortex circulation
ρ_A air density
ρ_W water density

We thank R. M. Alexander and P. Krueger for valuable intellectual input, M. McNitt-Gray, J. Carnahan, B. Valiferdowsi, and P. Masson for aid during model construction, D. Lauritzen and S. Bartol for assistance during data collection, and D. Dabiri, L. Zuhal, and D. Jeon for technical assistance. Smooth trunkfish were collected by W. Rosado, Department of Marine Science, University of Puerto Rico-Mayaquez. Financial support of the Office of Naval Research under contract N00014-96-0607 (to M.S.G. and M.G.) is gratefully acknowledged.

References

Aleyev, Y. G. (1977). *Nekton.* The Hague: Junk.

Anderson, E. J., McGillis, W. R. and Grosenbaugh, M. A. (2001). The boundary layer of swimming fish. *J. Exp. Biol.* **204**, 81-102.

Bannasch, R. (2000). Experimental studies on hydrodynamic adaptation in penguins – mechanisms of turbulence control and their applicability to engineering. *1st Int. Symp. Aqua Bio-mech./Int. Semin. Aqua Bio-mech.* **1**, 12-20.

Bartol, I. K., Gordon, M. S., Gharib, M., Hove, J. R., Webb, P. W. and Weihs, D. (in press). Flow patterns around the carapaces of rigid-bodied, multi-propulsor boxfishes (Teleostei: Ostraciidae). *Integ. Comp. Biol.* **42**.

Beal, D. N., Hover, F. S. and Triantafyllou, M. S. (2001). The effect of a vortex wake on the thrust and efficiency of an oscillating foil. *Proc. 12th International Symposium on Unmanned Untethered Submersible Technology (UUST01)*, Durham, NH, USA.

Bertin, J. J. and Smith, M. L. (1989). *Aerodynamics for Engineers*, 2nd edition. Englewood Cliffs: Prentice Hall.

Blake, R. W. (1977). On ostraciiform locomotion. *J. Mar. Biol. Assn UK* **57**, 1047-1055.

Blake, R. W. (1981). Mechanics of ostraciiform propulsion. *Can. J. Zool.* **59**, 1067-1071.

Blake, R. W. (1983a). *Fish Locomotion*. Cambridge: Cambridge University Press.

Blake, R. W. (1983b). Median and paired fin propulsion. In *Fish Biomechanics* (ed. P. W. Webb and D. Weihs), pp. 214-247. New York: Praeger.

Drucker, E. G. and Lauder, G. V. (1999). Locomotor forces on a swimming fish: three-dimensional vortex wake dynamics quantified using digital particle image velocimetry. *J. Exp. Biol.* **202**, 2393-2412.

Drucker, E. G. and Lauder, G. V. (2000). A hydrodynamic analysis of fish swimming speed: wake structure and locomotor force in slow and fast labriform swimmers. *J. Exp. Biol.* **203**, 2379-2393.

Drucker, E. G. and G. V. Lauder. (2001a). Locomotor function of the dorsal fin in teleost fishes: experimental analysis of wake forces in sunfish. *J. Exp. Biol.* **204**, 2643-2958.

Drucker, E. G. and Lauder, G. V. (2001b). Wake dynamics and fluid forces of turning maneuvers in sunfish. *J. Exp. Biol.* **204**, 431-442.

Dubois, A. B., Cavagna, G. A. and Fox, R. S. (1974). Pressure distribution of the body surface of swimming fish. *J. Exp. Biol.* **60**, 581-591.

Gordon, M. S., Hove, J. R., Webb, P. W. and Weihs, D. (2000). Boxfishes as unusually well-controlled autonomous underwater vehicles. *Physiol. Biochem. Zool.* **73**, 663-671.

Hove, J. R., O'Bryan, L. M., Gordon, M. S., Webb, P. W. and Weihs, D. (2001). Boxfishes (Teleostei: Ostraciidae) as a model system for fishes swimming with many fins: kinematics. *J. Exp. Biol.* **204**, 1459-1471.

Küchemann, D. (1978). *The Aerodynamic Design of Aircraft: A Detailed Introduction to the Current Aerodynamic Knowledge and Practical Guide to the Solution of Aircraft Design Problems.* New York: Pergamon Press.

Kramer, D. L. and McLaughlin, R. L. (2001). The behavioral ecology of intermittent locomotion. *Amer. Zool.* **41**, 137-153.

Land, M. F. (1999). Motion and vision: why animals move their eyes. *J. Comp. Physiol. A* **185**, 341-352.

Lisoski, D. (1993). Nominally 2-dimensional flow about a normal flat plate. PhD dissertation, California Institute of Technology.

Lorenson, W. E. and Cline, H. E. (1987). Marching cubes: a high resolution 3D surface construction algorithm. *ACM Comp. Graph.* **21**, 163-169.

McCormack, P. D. and Crane, L. (1973). *Physical Fluid Dynamics.* New York: Academic Press.

Müller, U. K., Smit, J., Stamhuis, E. J. and Videler, J. J. (2001). How the body contributes to the wake in undulatory fish swimming: flow fields of a swimming eel (*Anguilla anguilla*). *J. Exp. Biol.* **204**, 2751-2762.

Nauen, J. C. and Lauder, G. V. (2001). Locomotion in scombrid fishes: visualization of flow around the caudal peduncle and finlets of the chub mackerel *Scomber japonicus*. *J. Exp. Biol.* **204**, 2251-2263.

Noca, F., Shiels, D. and Jeon, D. (1997). Measuring instantaneous fluid dynamic forces on bodies, using only velocity fields and their derivatives. *J. Fluids Struc.* **11**, 345-350.

Pereira, R. and Gharib, M. (2002). Defocusing digital particle image velocimetry and the three-dimensional characterization of two-phase flows. *Meas. Sci. Technol.* **13**, 683-694.

Pereira, R., Gharib, M., Dabiri, D. and Modarress, D. (2000). Defocusing DPIV: a 3-component 3-D DPIV measurement technique. Application to bubbly flows. *Exp. Fluids* **29**, S078-S084.

Raffel, M., Willert, C. E. and Kompenhans, J. (1998). *Particle Image Velocimetry: A Practical Guide*. Berlin: Springer-Verlag.

Schlichting, H. and Truckenbrodt, E. (1969). *Aerodynamik des Flugzeuges*, Vol. 2, Ch. 7. Berlin: Springer-Verlag.

Stamhuis, E. J. and Videler, J. J. (1995). Quantitative flow analysis around aquatic animals using laser sheet particle image velocimetry. *J. Exp. Biol.* **198**, 283-294.

Tritton, D. J. (1998). *Physical Fluid Dynamics*, 2nd Edition. Oxford: Clarendon Press.

Tyler, J. C. (1980). Osteology, phylogeny, and higher classification of the fishes of the order Plectognathi (Tetraodontiformes). *NOAA Tech. Rep. NMFS Circular* **434**, 1-422.

Vogel, S. (1987). Flow-assisted mantle cavity refilling in jetting squid. *Biol. Bull.* **172**, 61-68.

Vogel, S. (1994). *Life in Moving Fluids*, 2nd Edition. Princeton: Princeton University Press.

Webb, P. W. (1998). Entrainment by river chub *Nocomis micropogon* and smallmouth bass *Micropterus dolomieu* on cylinders. *J. Exp. Biol.* **201**, 2403-2412.

Webb, P. W. (2000). Maneuverability versus stability? Do fish perform well in both? *1st Int. Symp. Aqua Bio-mech./Int. Semin. Aqua Bio-mech.* **1**, 21-29.

Webb, P. W. (2002). Control of posture, depth, and swimming trajectories of fishes. *Integ. Comp. Biol.* **42**, 94-101

Weihs, D. (1989). Design features and mechanics of axial locomotion in fish. *Amer. Zool.* **29**, 151-160.

Weihs, D. (1993). Stability of aquatic animal locomotion. *Cont. Math.* **141**, 443-461.

Weihs, D. (2002). Stability versus maneuverability in aquatic locomotion. *Integ. Comp. Biol.* **42**, 127-134.

Wilga, C. D. and Lauder, G. V. (1999). Locomotion in sturgeon: function of the pectoral fins. *J. Exp. Biol.* **202**, 2413-2432.

Wilga, C. D. and Lauder, G. V. (2000). Three-dimensional kinematics and wake structure of the pectoral fins during locomotion in leopard sharks *Triakis semifasciata*. *J. Exp. Biol.* **203**, 2261-2278.

Willert, C. E. and Gharib, M. (1991). Digital particle image velocimetry. *Exp. Fluids* **10**, 181-193.

Wolfgang, M. J., Anderson, J. M., Grosenbaugh, M. A., Yue, D. K. P. and Triantafyllou, M. S. (1999). Near-body flow dynamics in swimming fish. *J. Exp. Biol.* **202**, 2303-2327.